ACS Biomaterials SCIENCE & ENGINEERING

pubs.acs.org/journal/abseba

Article

Electrochemical Immunosensors Based on Zinc Oxide Nanorods for Detection of Antibodies Against SARS-CoV-2 Spike Protein in Convalescent and Vaccinated Individuals

Freddy A. Nunez, Ana C. H. Castro, Vivian L. de Oliveira, Ariane C. Lima, Jamille R. Oliveira, Giuliana X. de Medeiros, Greyce L. Sasahara, Keity S. Santos, Alexandre J. C. Lanfredi, and Wendel A. Alves*

Cite This: https://doi.org/10.1021/acsbiomaterials.2c00509

Read Online

ACCESS | Metrics & More | Article Recommendations | Supporting Information

ABSTRACT: Even after over 2 years of the COVID-19 pandemic, research on rapid, inexpensive, and accurate tests remains essential for controlling and avoiding the global spread of SARS-CoV-2 across the planet during a potential reappearance in future global waves or regional outbreaks. Assessment of serological responses for COVID-19 can be beneficial for population-level surveillance purposes, supporting the development of novel vaccines and evaluating the efficacy of different immunization programs. This can be especially relevant for broadly used inactivated whole virus vaccines, such as CoronaVac, which produced lower titers of neutralizing antibodies. and showed lower efficacy for specific groups such as the elderly and immunocompromised. We developed an impedimetric biosensor based on the immobilization of SARS-CoV-2 recombinant trimeric spike protein (S protein) on zinc oxide nanorod (ZnONR)-modified fluorine-doped tin oxide substrates for COVID-19 serology testing. Due to electrostatic interactions, the negatively charged S protein was immobilized via physical adsorption. The electrochemical response of the immunosensor was measured at each modification step and characterized by scanning electron microscopy and electrochemical techniques. We successfully evaluated the applicability of the modified ZnONR electrodes using serum samples from COVID-19 convalescent individuals, CoronaVac-vaccinated with or without positive results for SARS-CoV-2 infection, and pre-pandemic samples from healthy volunteers as controls. ELISA for IgG anti-SARS-CoV-2 spike protein was performed for comparison, and ELISA for IgG anti-RBDs of seasonal coronavirus (HCoVs) was used to test the specificity of immunosensor detection. No cross-reactivity with HCoVs was detected using the ZnONR immunosensor, and more interestingly, the sensor presented higher sensitivity when compared to negative ELISA results. The results demonstrate that the ZnONRs/spike-modified electrode displayed sensitive results for convalescents and vaccinated samples and shows excellent potential as a tool for the population's assessment and monitoring of seroconversion and seroprevalence.

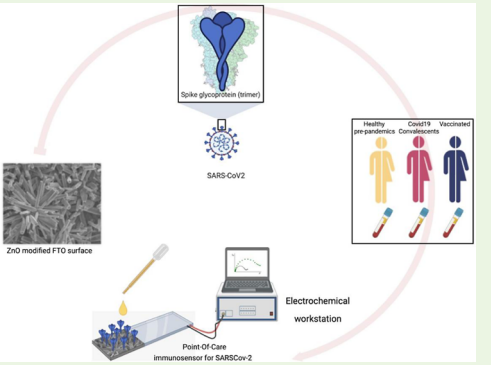

KEYWORDS: *COVID-19, SARS-CoV-2, electrochemical immunosensors, zinc oxide, serological diagnosis, immunosurveillance, CoronaVac*

INTRODUCTION

The coronavirus disease (COVID-19) pandemic has been a global health crisis for 2 years, causing over 456 million infections and more than six million deaths.[1] Several studies have been conducted to establish the seroprevalence of SARS-CoV-2 among the general population.[2−4] Vaccination against COVID-19 continues to be the most effective method of preventing severe disease, hospitalization, and death during the current pandemic, including those associated with the Omicron variant.[5,6]

Mass vaccination campaigns to prevent Covid-19 are now being conducted worldwide, with different types of vaccines, such as viral vector-based vaccines,[7] mRNA-based,[8] and inactivated virus vaccines.[9] The most widely used inactivated virus vaccine is the CoronaVac,[10,11] used especially in low- and middle-income countries.[12] Several studies reported very low vaccine-induced antibody titers in CoronaVac-vaccinated individuals.[12−15] Accurate and accessible seroprevalence detection may be of particular interest to public health activities in countries where this vaccine has been primarily used in vaccination programs.

Received: May 3, 2022
Accepted: August 24, 2022

Tests to detect seroprevalence in the general population to COVID-19 are critical to evaluate the effectiveness of vaccination programs, support the development of vaccines, and contribute to our understanding of the extent of infection among individuals who were not identified through active case finding and surveillance efforts, determining the attack rate in the population and the infection fatality rate.[16] The conventional methodology for serological determinations includes the traditional enzyme-linked immunosorbent assay (ELISA),[17] immunochromatographic Lateral flow assay (LFA),[18] and electrochemical biosensors.[19,20]

Methods based on electrochemical biosensors have been explored as promising alternatives for real-time monitoring of COVID-19.[21] Such devices feature a high level of sensitivity, specificity, operability, cost-effectiveness, miniaturization, and expeditious testing. They also decrease the need for costly equipment, specialized personnel, and extensive sample preparation. Such aspects make them useful diagnostic tools since they provide rapid and accurate results.[22,23]

One of the nanomaterials widely employed for biosensor production in recent years is zinc oxide (ZnO). This n-type semiconductive material features a broad energy gap (Eg = 3.37 eV) and a large exciton binding ability (60 meV).[24] With its unique chemical, optical, and electrical properties, added to its easy manufacturing in nanostructures of several sizes and morphologies, this metal oxide is a highly versatile material that has gained the attention of researchers not only for the development of electrochemical biosensors but also for electronic and optoelectronic devices, solar cells and supercapacitors, and biomedical applications.[25,26]

Indeed, ZnO can now be grown as bulk crystals, thin films, and nanostructures with various techniques[27] such as wet chemical method,[28] microwaves,[29] sputtering,[30] vapor deposition,[31−33] and electrodeposition.[34−36] This advancement has enabled its usage as a biosensor component, offering a high degree of reproducibility, scalability, design flexibility, and multiplexing of operational features. Some successful examples of practical device enhancement are the manufacturing of miniaturized micro−nano electrodes in glucose and urea sensors,[37−39] bacterial meningitis detection,[40] cholesterol biosensing,[41] H1N1 influenza detection,[42] legionella pneumophila diagnosis,[43] grapevine virus detection,[44] cancer diagnosis,[45,46] and many other devices employed as promising immunosensors.[47−52]

The high isoelectric point (IEP 9.5) of ZnO nanostructures makes them suitable for adsorbing materials with lower isoelectric points such as enzymes and proteins by the electrostatic interactions.[40,53] A positively charged ZnO matrix offers a receptive microenvironment for the negatively charged proteins or enzymes to maintain their activity. It significantly promotes the direct electron transport between the enzyme/protein and the electrode.[54] Several ZnO nanostructures have been prepared with shape controllers, such as urchin-like,[55] flower-like,[56] nanoplates,[57] nanorods,[58] and nanobelts.[59] The zinc oxide can occur in one-dimensional (1D), two-dimensional (2D), and three-dimensional (3D) structures.[60]

In this study, we have successfully developed ZnO nanorods functionalized with SARS-CoV-2 recombinant trimeric spike protein for electrochemical immunoassay of SARS-CoV-2 antibody detection tests. The platform distinguished in impedance measurement serum samples from naturally infected and vaccinated individuals with inactivated SARS-CoV-2 vaccine (CoronaVac) from negative control samples and was also capable of detecting seroconversion in samples from individuals previously considered seronegative by the standard ELISA test, with high sensitivity. There was no cross-reactivity for common human coronavirus (HCoV), demonstrating excellent specificity. These hierarchical electrodes based on ZnONRs can be used as an inexpensive surface substrate or electrode for seroprevalence determination, control, and monitoring of COVID-19.

MATERIALS AND METHODS

Materials. Zinc nitrate hexahydrate ($Zn(NO_3)_2{\cdot}6H_2O$, reagent grade 98%), hexamethylenetetramine (HMTA, ACS reagent ≥99%), glycine (ACS reagent ≥98.5%), potassium ferricyanide (ACS reagent, ≥99%), and potassium ferrocyanide (ACS reagent 98.5%) were obtained from Sigma-Aldrich. Potassium chloride (reagent grade 99%) was purchased from Labsynth. The SARS-CoV-2 recombinant trimeric spike protein has been kindly supplied by the Cell Culture Engineering Laboratory (LECC) of COPPE/Federal University of Rio de Janeiro. The monoclonal anti-SARS coronavirus recombinant human antibody, Clone CR3022 (produced in HEK293 cells), NR-5248 was made under HHSN272201400008C and obtained through BEI Resources, NIAID, NIH.

A total of 107 human blood serum samples were analyzed, divided into four groups: Pre-pandemic (N = 15), convalescents (N = 47) with polymerase chain reaction diagnostic confirmation at least 40 days after the onset of COVID-19 symptoms, CoronaVac-vaccinated individuals (without previous positive results for COVID-19 disease) (N = 25), and CoronaVac-vaccinated previously infected individuals (with a previous positive result for COVID-19 disease and vaccinated after that) (N = 20). All vaccinated individuals received two doses of a 3 μg vaccine/shot each, 4 weeks apart. Serum from convalescent individuals and CoronaVac-vaccinated individuals was processed at the Heart Institute Immunology Laboratory—InCor/HC-FMUSP. All convalescents and CoronaVac-vaccinated volunteers signed written informed consent approved by the Ethics Committee in Research of the Clinics Hospital of the University of Sao Paulo Medical School. (CAPPesq CAAE30155220.3.0000.0068). The BCRJ cell bank supplied serum from pre-pandemic individuals through approval by the Ethics Committee of the Federal University of ABC (CAAE—43139921.2.0000.5594). The samples were classified along with the article as prepandemic, convalescents, CoronaVac-vaccinated, and CoronaVac-vaccinated previously infected and stored at −80 °C until subsequent use.

ZnONR Preparation Processes. Fluorine-doped tin oxide (FTO) glasses were used as substrates to produce ZnONR films. The 1 × 1.5 cm-dimensioned substrates were washed three times by sonication in ethanol, deionized water, and acetone for 15 min. A two-step methodology based on the literature has been applied to grow the films, with minor modifications.[61] First, a seed layer was prepared by dripping aqueous solutions of $Zn(NO_3)_2$ (20 μL, 0.5 mol L^{-1}) and HMT (20 μL, 0.5 mol L^{-1}) on the substrates. After 5 min of deposition, the substrates were spin-coated for 6 s at 500 rpm and then for 30 s at 3000 rpm. Finally, they were annealed at 200 °C for 15 min. In the second step, the ZnONR films were grown hydrothermally by soaking the modified substrates in a mixture of $Zn(NO_3)_2$ (0.1 mol L^{-1}) and HMT (0.1 mol L^{-1}), keeping their volume ratio at 1:1 (v/v). The hydrothermal growth was performed at 100 °C for 4 h in a sealed beaker. The final modified electrode was called FTO-ZnONRs.

Fabrication of the Electrochemical Immunosensor. The FTO-ZnONR electrode was first rinsed with a phosphate buffer solution to generate a hydrophilic surface; then, 20 μL of SARS-CoV-2 recombinant spike protein (4 μg mL^{-1}) diluted in phosphate buffer (pH 7.4) was placed onto the FTO-ZnONR surface for adsorption. The drop was in contact with the ZnONR surface for 5 h, rinsed to remove any unbound protein, and dried (FTO-ZnONRs/spike). A glycine solution (10 μmol L^{-1}) was used as a blocking solution to minimize the non-specific adsorption; 20 μL was placed on the sample and left to react for 30 min, and the device was again washed

https://doi.org/10.1021/acsbiomaterials.2c00509
ACS Biomater. Sci. Eng. XXXX, XXX, XXX−XXX

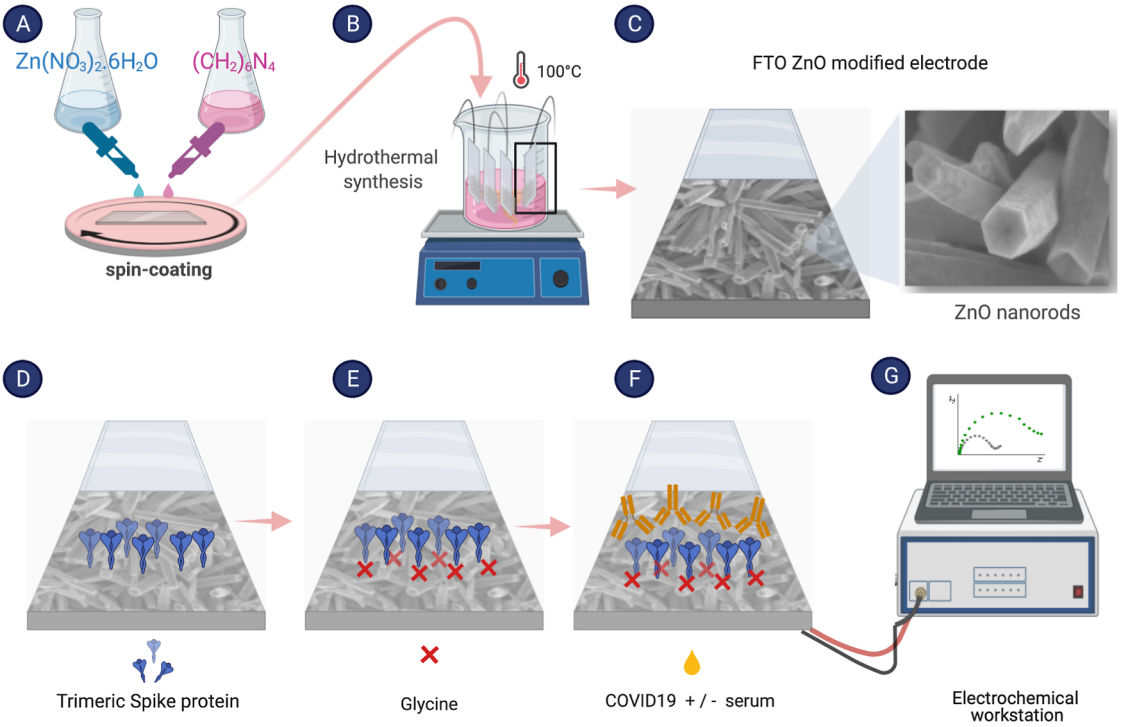

Figure 1. Schematic representation of the electrochemical ZnO immunosensor fabrication for anti-SARS-CoV-2 antibody detection. (A) Two-step method for ZnONR synthesis: In the first step, using a spin coater, a seed layer is added by dripping $Zn(NO_3)_2$ and HMT aqueous solutions on the FTO substrate, (B) hydrothermal method promotes the ZnONR film growth on the FTO surface at 100 °C, (C) modified electroactive surface (scanning electron microscopy highlighting the structure of ZnONRs on the FTO surface), (D) addition of SARS-CoV-2 recombinant trimeric spike protein (4 μg mL^{-1}), (E) surface blocking step is performed with glycine solution (10 μmol L^{-1}) to minimize the non-specific adsorption, (F) positive (containing anti-SARS-CoV-2 antibodies) or negative (pre-pandemic) serum samples (1:500 v/v) are placed on the ZnO electrode surface, and (G) read out is performed using an electrochemical workstation.

and dried (FTO-ZnONRs/spike/Gly). After that, 20 μL of blood serum diluted in phosphate buffer (pH 7.4) at a ratio of 1:500 (v/v) was incubated on the electrode surface and then stored for 1 h, rinsed next, and dried (FTO-ZnONRs/spike/Gly/serum). A schematic of the biosensor assembly process is shown in Figure 1. The positive samples (FTO-ZnONRs/spike/Gly/+serum) were analyzed with serum from convalescent and vaccinated individuals, while the negative samples (FTO-ZnONRs/spike/Gly/-serum) were analyzed with serum from prepandemic individuals.

Electron Microscopy and Spectroscopic Characterizations. Scanning electron microscopy (SEM) images were collected using a field-emission scanning electron microscope JMS-6701F (JEOL) situated in the Multiuser Experimental Center of the Federal University of ABC (CEM/UFABC, Santo André, Brazil) with a voltage of 5 kV. The solutions were diluted to the minimum possible concentration to observe the changes on the ZnONR surface and to carry out the observations on a microscope after each immunosensor assembly stage.

Fourier transform infrared spectroscopy (FTIR, Perkin Elmer) was recorded from 700 to 1800 cm^{-1} at room temperature with a spectral resolution of 4 cm^{-1} and an average of 124 data acquisitions. X-ray photoelectron spectroscopy (XPS; ThermoFisher Scientific, K-alpha +) was acquired with monochromatic Al Kα radiation. Carbon (C 1s) was used to calibrate the sample charging for XPS measurements. XPS data were processed using CasaXPS processing software.

Electrochemical Measurements. The electrochemical measurements were conducted with a μAutolab type III potentiostat/galvanostat for Metrohm, using NOVA 2.1 software supplied by Metrohm. In a conventional three-electrode system, an FTO-ZnONR-modified electrode was regarded as a working electrode, a platinum wire as a counter electrode, and a saturated calomel electrode as a reference electrode against which all potentials were measured. The response readings were performed in 5 mmol L^{-1} $K_4Fe(CN)_6/K_3Fe(CN)_6$ in 0.1 mol L^{-1} KCl (pH 7.3).

Enzyme-Linked Immunosorbent Assay. The ELISA was performed using 96-well high-binding half-area polystyrene plates (Corning, USA) coated overnight at 4 °C with 4 μg mL^{-1} spike protein and diluted in carbonate−bicarbonate buffer (pH 9.6, 0.1 mol L^{-1}). For cross-specificity experiments using pre-COVID-19 pandemic serum samples, plates were coated with 4 μg mL^{-1} RDB proteins of the four endemic human CoVs (229E, OC43, NL63, and HKU1). All HCoV proteins used for ELISA were kindly provided by Boscardin's Laboratory (ICB-USP). After this period, the coating solutions were discarded, and 80 μL of BSA (1%), skim milk powder (5%), and Tween-20 (0.05%) in phosphate-buffered saline (PBS) were added to each well for blocking, carried out at room temperature for 2 h. Serum or plasma samples were thawed at room temperature, incubated at 56 °C for 30 min to inactivate the virus, and diluted (1:100) in BSA (0.25%), skimmed milk powder (5%), and Tween-20 (0.05%) in PBS. 25 μL of this solution was added to each well and incubated at 37 °C for 45 min. After incubation, the plates were washed with Tween-20 (0.05%) in PBS five times. 25 μL of peroxidase-conjugated goat anti-human IgG secondary antibody solutions (Jackson Immunoresearch, USA) diluted 1:10,000 in BSA (0.25%), skim milk powder (5%), and Tween-20 (0.05%) in PBS were added to each well and incubated at 37 °C for 30 min and then washed five times. The *o*-phenylenediamine dihydrochloride tablets (Sigma, USA) were dissolved in phosphate−citrate buffer (pH 5.0, 0.05 mol L^{-1}) at a concentration of 0.4 mg mL^{-1}. Immediately before use, 5 μL of hydrogen peroxide (30%) was added to the solution. Then, 25 μL of the final solution was added to each well, and the plates were incubated in the dark at room temperature for 30 min. After incubation, the reaction was halted by adding 25 μL of a 2 N H_2SO_4 solution to each well. Plates were then read at 490 nm using a plate reader (GloMax, Promega, USA). All samples were run in

https://doi.org/10.1021/acsbiomaterials.2c00509
ACS Biomater. Sci. Eng. XXXX, XXX, XXX−XXX

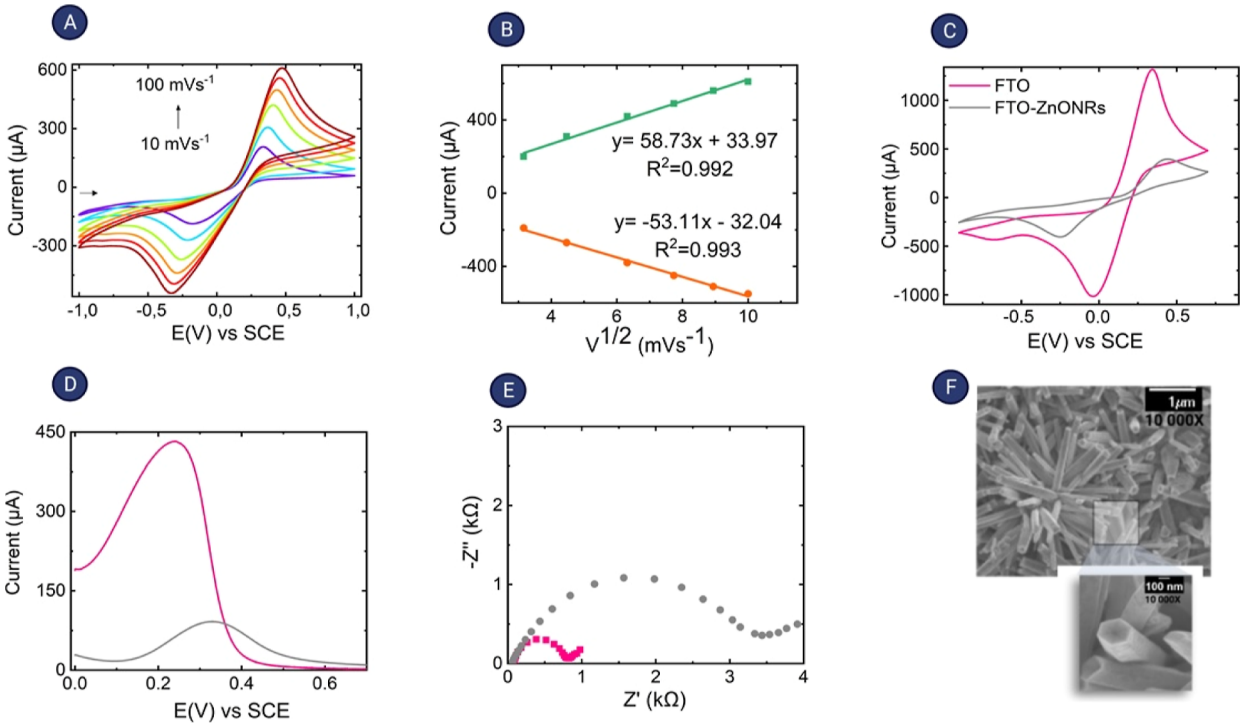

Figure 2. Functional modification of the FTO electrodes. (A) Cyclic voltammograms of the FTO-ZnONR electrode at different scan rates, varying from 10, 20, 40, 60, 80, and 100 mV s^{-1}, (B) plot of peak current versus square root of the scan rate of the FTO-ZnONR electrodes. (C) Cyclic voltammograms in a sweep window of −0.9 to 0.7 V at a scan rate of 50 mV s^{-1}, (D) square wave voltammograms in a sweep window of 0−0.7 V with a modulation amplitude of 20 mV and a frequency of 20 Hz, (E) Nyquist diagram of EIS measurements performed from 30 kHz to 0.1 Hz with an RMS amplitude of 10 mV, demonstrating the electrode surface of FTO (pink) and after functionalization with ZnONRs (Gray). (F) SEM images of the ZnONRs. Electrolyte: solution of 5 mmol L^{-1} $K_4Fe(CN)_6/K_3Fe(CN)_6$ in 0.1 mol L^{-1} KCl.

duplicate. Pre-COVID-19 samples were included as negative controls in the experiments. The values were determined as optical density minus blank, and results are given as the ratio of participant samples/average of a set of 20 control pre-pandemic samples. An antibody ratio of ≥1.2 was considered positive.

Statistical Analysis. Descriptive statistics, receiver operating characteristics (ROCs), and correlation analysis were performed using GraphPad Prism software version 9, and a p-value < 0.05 was considered statistically significant. The variables were analyzed using the Kruskal−Wallis test with Dunn's post-hoc test for multiple comparisons.

RESULTS AND DISCUSSION

Electrochemical Characterization of the FTO-ZnONR Electrode. Cyclic voltammetry (CV) is a powerful electrochemical technique used to assess the oxidation−reduction processes of molecular species and study chemical reactions initiated by electron transfer.[62] It is popularly used in the electrochemical characterization of materials due to its ease of execution and rapid analysis.[63] The electrochemical and morphological performance of the FTO electrode modified with ZnONRs was evaluated and is shown in Figure 2.

The linearity of anodic and cathodic peak currents versus the square root of the scan rate (Figure 2A,B) revealed an efficient diffusion-controlled process, demonstrating a thermodynamically favorable electron transfer with an improved electrochemical signal pattern. As the scan rate increases, oxidation and reduction peak current increases along with a gradual shift of the potential oxidation peak toward a positive direction and reduction rise toward a negative approach. This behavior indicates a limitation in the charge transfer kinetics, characteristic of a quasi-reversible system.[39,64] The observed peak separation potential, $\Delta E_p = (E_{pa} - E_{pc})$ of 90 mV, was more significant than the value expected for a reversible system. The reversible systems tend to have a peak-to-peak voltage difference of $59/n$ mV.[65] It is known that for reversible and diffusion-controlled systems, the peak is proportional to the scanning speed according to the Randles−Sevcik equation[66]

$$I_p = (2.69 \times 10^5) n^{3/2} A D^{1/2} C V^{1/2} \quad (1)$$

where: I_p is the peak current, n is the number of electrons transferred during the oxidation or reduction, A is the electroactive area of the electrode (cm^2), D is the coefficient of diffusion (cm^2 s^{-1}), C is the concentration of the electroactive species (mol/cm^3), and V is the scan rate (V s^{-1}). Rearranging the Randles−Sevcik equation, we can find the electroactive area of the electrode

$$A = \frac{I_p}{V^{1/2}} \times \frac{1}{2.69 \times 10^5 n^{3/2} D^{1/2} C} \quad (2)$$

Note that the first term refers to the angular coefficient of the lines obtained in the graph of peak current versus the square root of scan rate (Figure 2B) [Amps/(V $s^{-1})^{1/2}$]. The other variables are n = 1, $C = 5 \times 10^{-6}$ mol/cm^3, and the coefficient of potassium ferricyanide diffusion being equal to 6.39×10^{-6} cm^2 s^{-1}. An electroactive area value of 0.017 cm^2 was obtained for the FTO-ZnONR electrode. Similar results have been reported in the literature for the ZnO electrode surface area.[67,68] In contrast, an electroactive area value of 0.039 cm^2 was obtained for the bare FTO (Figure S1). As we can see, the bare FTO electroactive area is higher than that of

https://doi.org/10.1021/acsbiomaterials.2c00509
ACS Biomater. Sci. Eng. XXXX, XXX, XXX−XXX

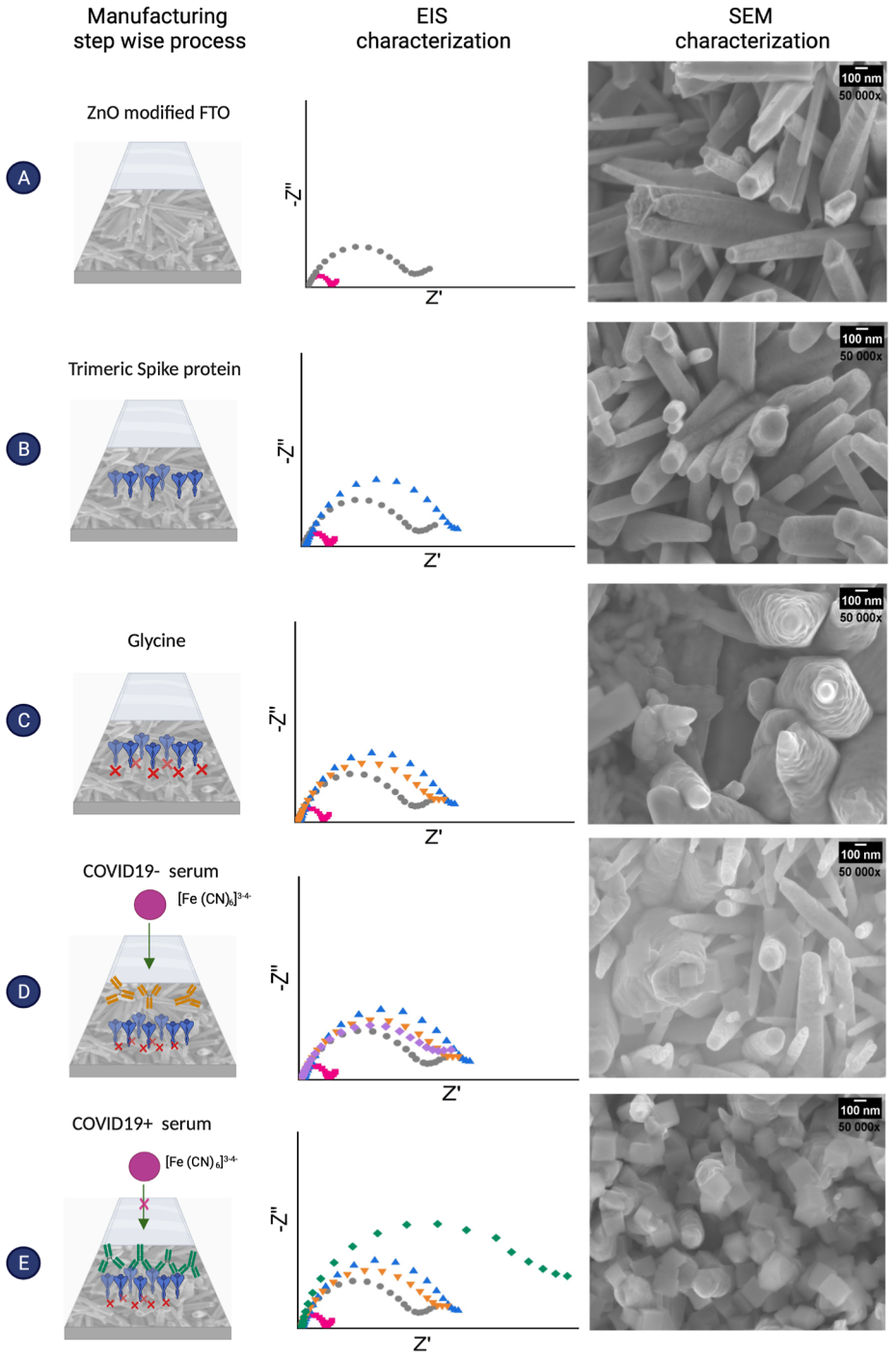

Figure 3. Electronic microscopy characterization of ZnONR immunosensors and EIS measurements at each assembly stage. (A) ZnONRs, (B) after S protein adsorption (4 ng mL^{-1}), (C) after glycine block (10 nmol L^{-1}), (D) in the presence of serum from the pre-pandemic individuals (1:1000 v/v), and (E) in the presence of serum from the convalescent individuals (1:1000 v/v).

FTO-ZnONRs, and it can be assigned to the ZnO semiconductor properties.[69,70]

On the other hand, CV significantly decreases the peak oxidation current from 1317 μA (bare FTO) to 395 μA after modification with ZnONRs (Figure 2C). We also observed in the square wave voltammetry (SWV) tests (Figure 2D) that the peak intensity had a reduction of approximately 70% with the addition of the nanomaterial, which promoted a shift of the peak to more positive potentials. The Nyquist diagram (Figure 2E) confirms the result that was observed in CV since it shows an increase in the R_{ct} signal from 0.65 kΩ (bare FTO) to 3.37 kΩ when the ZnONRs are deposited on the FTO electrode; similar results have been reported in the literature for electrochemical impedance spectroscopy (EIS) and CV experiments with ZnO electrodes.[40,71]

The results obtained by CV, SWV, and EIS suggest that the matrix of ZnONRs (Figure 2F) offers some resistive path for the flow of electrons from the electrolyte to the substrate. In contrast, a direct transfer of electrons is possible at the bare FTO electrode. However, the ZnO matrix has several advantages: biocompatibility, low toxicity, high electron mobility, chemical stability, high isoelectric point, and easy

https://doi.org/10.1021/acsbiomaterials.2c00509
ACS Biomater. Sci. Eng. XXXX, XXX, XXX−XXX

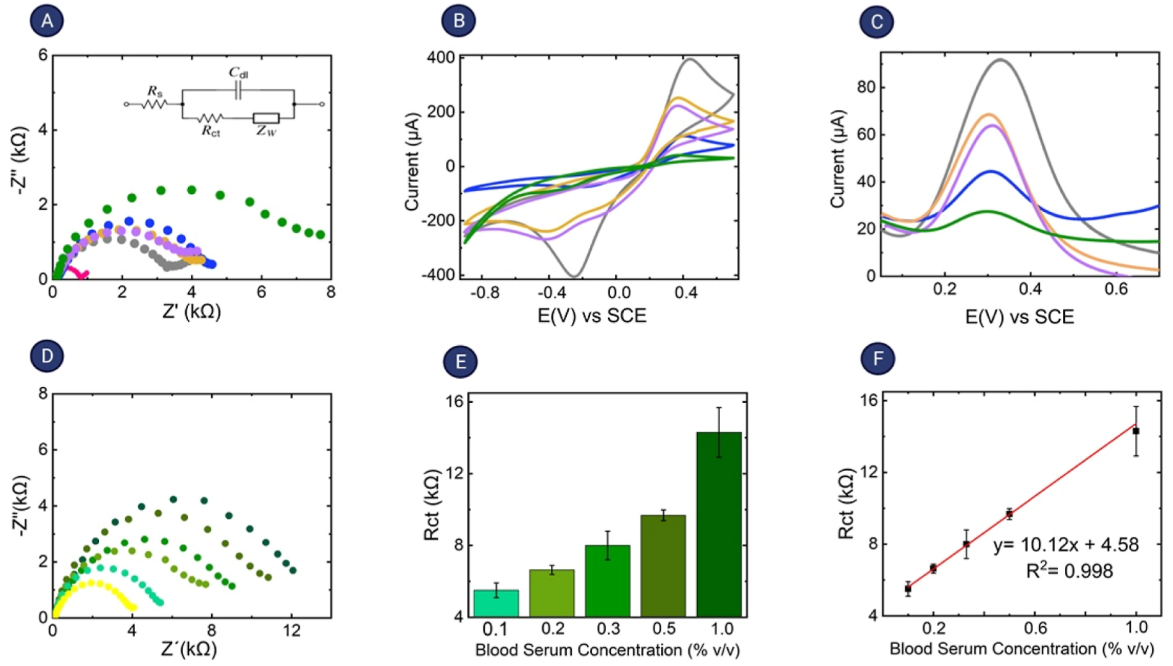

Figure 4. Electrochemical behavior and electrochemical validation of the ZnONRs/spike immunosensor. (A) Nyquist diagram of EIS measurements at each assembly stage performed from 30 kHz to 0.1 Hz with an RMS amplitude of 10 mV. Inset: the equivalent circuit model used for fitting the impedance data, (B) CV at each assembly stage, where the potential was swept from −0.9 to 0.7 V at a scan rate of 50 mV s^{-1}, (C) SWV, swept from 0 to 0.7 with a modulation amplitude of 20 mV and 20 Hz. Being (gray) ZnONRs, (blue) spike trimeric protein (4 μg mL^{-1}), (orange) glycine (10 μmol L^{-1}), (lila) serum from pre-pandemic, and (green) serum from convalescent individuals (1:500 v/v dilution), (D) Nyquist diagram of the calibration study by varying the concentration of positive serum-containing SARS-CoV-2 antibodies (green), dilutions were made in phosphate buffer being 0.1, 0.2, 0.33, 0.5, and 1 (%v/v) and shown in yellow the value refers to a blank (FTO-ZnONRs/spike/Gly), (E) bar graph showing the R_{ct} values obtained using the Nyquist diagrams and the Randles circuit as a function of the concentration of blood serum containing SARS-CoV-2 antibodies, and (F) calibration curve showing the variation of R_{ct} with the concentration of blood serum containing SARS-CoV-2 antibodies. Electrolyte: solution of 5 mmol L^{-1} $K_4Fe(CN)_6/K_3Fe(CN)_6$ in 0.1 mol L^{-1} KCl.

fabrication, turning it into a promising electrochemical biosensing platform.[37,39,54]

Working Principle of the Immunosensor. A method for directly connecting an electronic device to a biological environment is challenging due to the inherent complexity of biosensor development. Nanomaterials enable the miniaturization of devices, enhancing their sensitivity due to their higher surface area and long-range electron conductivity.[72,73] The ZnONRs create a favorable environment for biomolecules adsorption, maintaining their functionality and converting biological events into a stable, selective, and sensitive measurable signal. The SARS-CoV-2 recombinant trimeric spike protein was the biomolecule used to construct the electrochemical biosensing detection platform for anti-spike antibodies as the S protein is the main target antigen component from all structural proteins of SARS-CoV-2.[74] When working at physiological pH (7.4), the IEP of S protein (∼5) has a net negative surface charge, and the ZnONR matrix with a high isoelectric point (∼9.5) takes a net positive surface charge density. Thus, the negatively charged protein can be immobilized by electrostatic interaction on the surface of the positively charged ZnONR matrix. This principle has been widely used for the development of multiple immunosensors.[43,75−78]

The detection is achieved by measuring the Faradic impedance spectra for the ferro/ferricyanide redox couple $[Fe(CN)_6]^{3-/4-}$ after each modification step process of the electrode. Thus, the binding of anti-SARS-CoV-2 antibodies in human blood to the immobilized antigenic protein increases the R_{ct} signal. This increase is attributed to the electrode surface coverage with the bulky-sized antibodies. This coverage of the surface with the antibody retards the access of the ferro/ferricyanide redox couple to the conductive surface, reducing the electron transfer efficiency.

Electron Microscopy and Spectroscopic Characterizations. SEM images of ZnONRs show that the rods have a hexagonal shape with an average diameter of 490 nm, as shown in Figures 2F and 3A. The results are consistent with studies previously published by the group[61,79] and other researchers.[80−82] After SARS-CoV-2 recombinant spike protein immobilization, visual morphological changes were observed. The surface of the nanorods does not look smooth; it seems to be covered, indicating that an optimal immobilized protein profile was achieved (Figure 3B). Subtle modifications on the surface were observed after the blocking step with glycine (Figure 3C). Surprisingly, antigen−antibody complexes (anti-SARS-CoV-2 antibodies bound to immobilized spike proteins) induced dramatic morphological changes on the top of the electrode (Figure 3E). The electrode morphology modified with negative serum from pre-pandemic individuals is very similar to the surface where the spike protein is immobilized with glycine (blocking step), as shown in Figure 3D. This indicates that no SARS-CoV-2 antibodies were present in the tested pre-pandemic samples; consequently, no antigen recognition occurred.

Figure S2 shows FTIR spectra at each stage of device fabrication, and we also compare the spectra obtained in the presence of serum from the pre-pandemic and convalescent

https://doi.org/10.1021/acsbiomaterials.2c00509
ACS Biomater. Sci. Eng. XXXX, XXX, XXX−XXX

individuals in the range of 1800−700 cm^{-1}. The FTIR spectrum of the ZnO nanostructures shows a broad band around 1600 cm^{-1} and an absorption peak at 1116 cm^{-1} assigned to O−H stretching and deformation vibrations of adsorbed water on the ZnO surface, respectively.[83,84] The band at 1370 cm^{-1} can be correlated to NO_3 stretch, which also appeared at 831 cm^{-1} as a weak band.[85] The absorption bands at 1258 and 1203 cm^{-1} correspond to the stretching modes of HMTA used for the growth process of the ZnONRs.[80] The FTIR spectrum from spike-attached ZnONRs shows characteristic bands of amide-I (C═O stretching, 1600−1700 cm^{-1}), amide-II (N−H bending, 1500−1600 cm^{-1}), and amide-III (C−N stretching and N−H bending, 1200−1330 cm^{-1}), which indicates that protein is attached on the surface of the modified electrode.[86−88] In the presence of glycine, no significant change in the FTIR spectrum was observed due to the overlap with the spike protein bands. Also, in the presence of negative serum, the vibrational spectra are very similar to the spike protein immobilized with glycine on the electrode ZnONR surface, as shown in Figure 3D, which correlates with SEM images and EIS spectra (Figure 3D), confirming no interaction has occurred. However, for convalescent serum, a significant increase in the bands at 1560−1464 cm^{-1} associated with IgG, 1420−1289 and 1160−1028 cm^{-1} related to IgM, and 1285−1237 cm^{-1} designed to IgA were detected.[87] These bands were broad and overlapping in the spectrum of the spike-immobilized electrode surface, which can evidence the conjugation of antibodies to the FTO-ZnONRs/spike/Gly interface.

XPS analysis of ZnO electrodes revealed the presence of nitrogen on the surface after functionalization, indicating successful spike protein attachment (Figure S3).[89−91] Furthermore, it is possible to observe an increase in N 1s peak with the incubation of the antibodies anti-SARS-CoV-2 present in human samples (FTO-ZnONRs/spike/Gly/+serum electrode), revealing the binding of antibodies to the electrode surface (Figure S3A). Figure S3B shows the high-resolution spectra for the FTO-ZnONR electrode. The binding energies were calibrated using the carbon C 1s peak (284.6 eV). The high-resolution Zn 2p spectrum peaks at 1043.28 and 1020.18 eV correspond to Zn $2p_{1/2}$ and Zn $2p_{3/2}$, respectively. The binding energy variation determined from the XPS study was ∼23 eV, confirming that Zn atoms were in a Zn^{2+} oxidation state.[92,93] The O 1s high-resolution spectrum exhibited two Gaussian peaks named O1 and O2. The O1 peak at ∼529 eV is related to O^{2-} ions in the wurtzite structure of the hexagonal Zn^{2+}-ion array.[94−96] The peak O2 at 530.78 eV can be attributed to the OH group adsorbed on the surface of the ZnONRs.[94,95] Figure S3C shows the high-resolution core-level spectra of C 1s at each fabrication stage of the electrode, and the peak at 284.6 eV can be attributed to C−C. The binding energy peaks at 286 and 288 eV are related to C−O and C═O bonds, respectively.[97,98] The N 1s high-resolution core-level spectra (Figure S3D) exhibit two peaks at 399 and 400, which can be attributed to the C−N/N═C and N−C═O bonds, respectively.[98] Figure S3E shows the high-resolution core-level spectra of O 1s, where a peak located at 531 eV can be assigned to C═O, the peak at 532 eV can be assigned to C−OH, and the peak at 533 eV can be assigned to O−C═O/O−C−O.[97]

Electrochemical Response Studies of the ZnONRs/Spike Immunosensor. The EIS, CV, and SWV were used to characterize the electrode at each manufacturing stage (Figure 4). It shows the Faradic impedance spectra for the redox of $[Fe(CN)_6]^{3-/4-}$ measured at each manufacturing stage. The imaginary impedance component (Z'') is displayed as a function of the real component of impedance (Z'), as shown in Figure 4A.

These impedance spectra are typical of the theoretical, semicircular shape observed when the data is modeled using a Randles equivalent circuit, a helpful tool for analyzing EIS data that accounts for the resistive and capacitive processes at different frequencies.[99] A modified Randles circuit (inset in Figure 4A) with a constant phase element simulated the experimental diagrams. This equivalent circuit's components are R_s, the electrolytic resistance between the modified working electrode and the Pt reference electrode, and C_{dl}, the double-layer capacitance. Also, W is the Warburg impedance, and R_{ct} is the charge transfer resistance of the $[Fe(CN)_6]^{3-/4-}$ redox probe. In the Faradic impedance measurements, R_{ct} is the most sensitive parameter to describe the electrodes' surface recognition process.[100] As was previously mentioned, the R_{ct} value of the FTO electrode increases from 0.65 kΩ for bare FTO to 3.37 kΩ for FTO-ZnONRs. Despite this increase in the R_{ct} signal, using the ZnONR matrix is advantageous because it provides a biocompatible environment suitable for immobilizing enzymes, proteins, and DNA.[27] Then, after immobilization of SARS-CoV-2 recombinant trimeric spike protein, the semicircle area increases to 4.66 kΩ (FTO-ZnONRs/spike), which can be related to the barriers created on the electrode surface. This increase in the R_{ct} signal suggests that the recombinant spike protein was successfully immobilized on the electrode surface.

The R_{ct} value of the FTO-ZnONRs/spike/Gly was 3.98 kΩ, which is less than that for the FTO-ZnONRs/spike electrode (4.66 kΩ), which can be related to the difference in charge on the surface after attachment of the glycine molecules, which decreases the resistance to the charge transfer. Regarding the negative serum, the R_{ct} signal obtained was 3.99 kΩ (FTO-ZnONRs/spike/Gly/-serum), very similar to the FTO-ZnONRs/spike/Gly signal, suggesting that glycine prevented non-specific interactions, as expected. After dripping the positive serum on the electrode surface (FTO-ZnONRs/spike/Gly/+serum), the semicircle area increases significantly to 6.72 kΩ. It is assigned to the electrode surface coverage with the bulky-sized antibodies (an average molecular weight of approximately 150 kDa[101]). This surface coverage with the antibody reduces the electron transfer efficiency, increasing the R_{ct}. This significant increase in the R_{ct} signal suggests that the antibodies present in the blood serum recognize the S protein immobilized on the electrode surface. Table S1 summarizes the R_{ct} values obtained in each step of the developed immunosensor.

The results obtained in the CV and SWV were confirmed by EIS measurements, as shown in Figure 4B,C. A significant decrease in peak current was observed in the presence of antibodies due to the barriers created on the electrode surface. The bulky protein and antibody retard the redox molecules from reaching the surface. The current increases in the cathodic peak current for the electrode after the attachment of the glycine layer, which can be attributed to the amount of charge variation after the attachment of blocking molecules to the film's surface, affect the mobility of charge carriers of the mediator.

Analytical Sensitivity Analysis. The impedimetric response to different dilutions of human serum samples was

https://doi.org/10.1021/acsbiomaterials.2c00509
ACS Biomater. Sci. Eng. XXXX, XXX, XXX−XXX

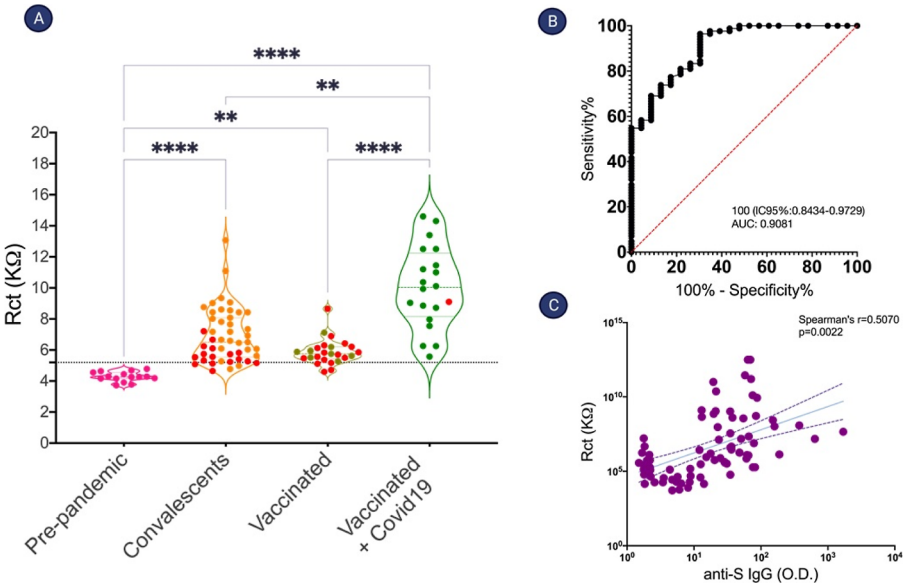

Figure 5. Detection accuracy of the developed electrochemical ZnONRs/spike immunosensor. (A) ZnONRs/spike immunosensor response was compared among a representative set of clinical samples from healthy pre-pandemic individuals, convalescents, and CoronaVac-vaccinated individuals. Serum samples were analyzed using the electrochemical impedance method and data were expressed in charge transfer resistance (R_{ct}). Red color dots indicated previously considered negative samples in anti-S IgG by ELISA test, (B) ROC curve was used to describe the discrimination accuracy of the developed electrochemical immunosensor, and (C) correlations between total antibody response against the SARS-CoV-2 spike protein measured from charge transfer impedance (R_{ct}) via our ZnONRs/spike immunosensor and IgG antibodies against the SARS-CoV-2 spike protein (anti-S IgG) detected using conventional ELISA, in all positive samples analyzed (healthy pre-pandemics, convalescents, and vaccinated individuals).

performed through successive titration to validate the ZnONRs/spike immunosensor for detecting anti-S antibodies in clinical samples. The sera were diluted with phosphate buffer (pH 7.4). The error bars corresponded to the standard deviation of the data points in triple experiments. EIS results are shown in Figure 4D, which presents the Nyquist diagram. The system indicates that the impedance increases with the concentration of the target analyte. The R_{ct} signal increases from 3.98 kΩ for the blank (FTO-ZnONRs/spike/Gly) to 5.04 kΩ after adding serum with a concentration equal to 0.1% v/v. To add a dilution of 0.2% v/v serum, the R_{ct} increases to 6.77 kΩ, and it continues to grow until showing an R_{ct} signal of 13.5 kΩ to add a serum with a concentration of 1.0% v/v. This trend evidences the binding of the antibodies present in human serum to the antigen immobilized on the electrode surface, increasing the hindrance to the movement of redox molecules. The R_{ct} values of the different EIS plots exhibited linear associations, as shown in Figure 4E,F. For the concentration range of 0.1−1% v/v, the correlation coefficient (R) was 0.998. It demonstrates that the biosensor signal is specific and works dose-dependently using a range of blood serum samples containing anti-SARS-CoV-2 spike protein antibodies.

The quantification detection of monoclonal antibodies (mAbs) anti-SARS-CoV spike protein (Clone: 3022) was performed under optimal conditions. EIS results are shown in Figure S2, which presents the Nyquist diagram (Figure S4A). The system clearly shows that the impedance increases with the concentration of the target analyte (Figure S4B). The R_{ct} values of the dose−response curve of IgG mAb were plotted against the IgG mAb concentration (Figure S4C). The linear response of antibodies ranges from 200 to 1200 ng mL^{-1}. The correlation coefficient (R) was calculated to be 0.995. The limit of detection (LOD) was 19.34 ng mL^{-1} using the equation[102]

$$\mathrm{LOD} = 3.3 \times \left(\frac{\mathrm{SD}}{\mathrm{slope}}\right) \quad (3)$$

the value of SD is the standard deviation of the blank FTO-ZnO/spike/Gly bioelectrode under control conditions. The limit of quantification (LOQ) was 58.62 ng mL^{-1} using the equation[103]

$$\mathrm{LOQ} = 10 \times \left(\frac{\mathrm{SD}}{\mathrm{slope}}\right) \quad (4)$$

This biosensor's sensitivity is adequate for detecting COVID-19 seroconversion and was comparable and even better than other immunoassays (Table S2).[20,104−107] Moreover, the device is portable, cheaper, and has shown a great potential to evaluate the humoral immune response in COVID-19 convalescent individuals or post-COVID-19 vaccinated individuals, offering an affordable and powerful alternative compared to the existing COVID-19 serological assays.

Determination of Positive/Negative Cutoff Threshold of Anti-SARS-CoV-2 Antibodies in Clinical Samples. The analytical validation began by establishing a cutoff point or a positive/negative threshold defined as the level of antibody activity that determines the positive or negative reactive status for a serum/plasma sample from a given individual.[108] In this case, the result is positive when a test serum presents an R_{ct} (kΩ) value above that determined in the cutoff. Still, if the result is below the cutoff value, the sample is deemed negative for SARS-CoV-2 antibodies. The cutoff determination was made considering the distribution of the R_{ct} resulting from the analysis of the 15 negative human blood samples (Figure 5A), following the formula below[109]

https://doi.org/10.1021/acsbiomaterials.2c00509
ACS Biomater. Sci. Eng. XXXX, XXX, XXX−XXX

$$\text{Cut} - \text{off} = \overline{X} + 3 \times \text{SD} \quad (5)$$

where $\overline{X}$: mean and SD: standard deviation. The value obtained for the cutoff was 5.20 kΩ.

Diagnostic Sensitivity, Specificity, and Determination of Anti-SARS-CoV-2 Antibodies in Clinical Serum Samples. The performance of the developed sensor in detecting the presence of spike SARS-CoV-2 antibodies in clinical samples was determined by analyzing 47 blood serum samples from individuals previously infected and recovered from SARS-CoV-2 (convalescent individuals). Figure 5A shows the R_{ct} obtained from pre-pandemic and convalescent samples with the calculated cutoff (dotted black line). The graphic reveals that the sensor identified the COVID-19 serum samples selectively and exhibited a relevant increase in R_{ct} values compared to pre-pandemic samples. Consequently, the ZnONRs/spike immunosensor discriminated between COVID-19 convalescent (positive) and pre-pandemic (healthy negative) samples. The immunosensor showed a negligible response toward the samples collected from pre-pandemic individuals, which suggests that no SARS-CoV-2 antibodies are found that can bind to the S protein. However, the positive confirmed clinical samples showed a significant relative change in the R_{ct} values. Although all the samples were from convalescent individuals, differences in R_{ct} signals were observed, attributed to the number of antibodies in the samples. The immune response will depend on each person since it is influenced by intrinsic and environmental factors, such as age, sex, genetics, and lifestyle.[11,110] Some individuals can react by getting excellent antibody levels against the SARS-Cov-2 virus, while others do not. Afterward, not all SARS-CoV-2-infected individuals will develop detectable antibodies using regular SARS-CoV-2 antibody tests. For these reasons, we observed a heterogeneous response in our study. Therefore, the antibody levels present in the samples that can effectively bind to the S protein immobilized on the electrode surface is variable for each sample. A higher R_{ct} signal could be interpreted as a more significant number of antibodies in the analyzed samples.

On the other hand, the biosensor was developed to detect positive samples for anti-SARS-CoV-2 spike protein antibodies, even in the negative samples in the ELISA plate wells (Figure S5), which is considered a gold standard test to perform serological diagnosis. Therefore, the diagnostic sensitivity and specificity values were calculated with a defined cutoff, and positive and negative samples were analyzed. For this, the following formulas were used[111]

$$\text{sensitivity} = \left[\frac{a}{(a + c)}\right] \times 100 \quad (6)$$

$$\text{specificity} = \left[\frac{d}{(b + d)}\right] \times 100 \quad (7)$$

where a: true-positive, b: false-positive, c: false-negative, and d: true-negative.

The sensitivity is the proportion of individuals with the disease who are accurately diagnosed with a positive test result ("true-positive rate"). In contrast, specificity is the proportion of individuals without the disease who are precisely identified by a negative test result ("true-negative rate").[112] The sensitivity and specificity values for the immunosensor described in this work were 88.7, and 100%, respectively.

Serological Cross-Reactivity with Common Coronavirus (HCoVs) Assessment. A suitable COVID-19 serological sensor must be sensitive and highly specific, ruling out any cross-reactivity with similar coronaviruses such as seasonal endemic HCoVs.[113] Therefore, the seroconversion of HCoVs in pre-COVID-19 pandemic serum samples was evaluated using ELISA to detect specific IgG antibodies against the RDB proteins of the four most common HCoVs (229E, OC43, NL63, and HKU1). ELISA results showed that all pre-pandemic samples analyzed in this study were positive for HCoVs (Figure S6). Simultaneously, using the ZnONRs/spike immunosensor, 100% of the same pre-COVID-19 cohort was found negative, demonstrating that our sensor is precise for SARS-CoV-2. It successfully distinguished the negative samples and eliminated the adverse risk of cross-specificity with human antibodies against HCoVs.

Detection of SARS-CoV-2 Antibodies in Vaccinated Individuals with Inactivated SARS-CoV-2 Vaccine (CoronaVac). To evaluate the applicability of the developed sensor in detecting anti-SARS-CoV-2 antibodies in vaccinated individuals, we analyze 45 human blood serum samples from individuals vaccinated with inactivated SARS-CoV-2 vaccine (CoronaVac vaccine) at least 28 days after the second immunization. From these 45 samples, 25 were from CoronaVac-vaccinated individuals (without previous positive results for COVID-19 disease) and 20 from CoronaVac-vaccinated, previously infected individuals (with a previous positive result for COVID-19 disease). Figure 5A shows the R_{ct} results, demonstrating that the sensor responds to blood serum and increases the R_{ct} values compared to pre-pandemic samples previously tested. It means that our ZnONRS/spike immunosensor could identify the antibody-induced response against SARS-CoV-2 spike protein stimulated by CoronaVac vaccination.

Vaccinated samples presented more homogeneous antibody-induced immune responses. Only slight variation in the R_{ct} values was found compared to that in samples from convalescents. This behavior might be justified because of the higher variability of naturally triggered humoral responses post-viral infection compared to vaccine-induced humoral immunity.[114,115]

The ZnONRs/spike immunosensor readouts (R_{ct} signal) from previously infected individuals followed by two vaccine doses have shown significantly higher R_{ct} values than those from asymptomatic or negative individuals without positive results COVID-19 disease before the immunization protocol, following data already reported.[116]

Our results confirmed recently described data where administration of the inactivated SARS-Cov-2 vaccine, CoronaVac, also induced higher antibody responses in previously naturally infected individuals.[117] According to Wang et al.[118] is expected that vaccination increases all components of the humoral response due to the ongoing antibody somatic mutation, memory B cell clonal turnover, and other general intrinsic factors related to vaccine-induced humoral immune responses.

It is essential to highlight that 16 samples of the 45 analyzed were negative for anti-SARS-CoV-2 spike protein antibodies by ELISA test (Figure S5), with the ZnONRs/spike immunosensor, and 12 samples showed a positive result, showing that the modified electrode has a higher sensitivity and efficiency than the golden standard tests. We can also highlight that the R_{ct} signal for some of these samples was slightly higher than the

https://doi.org/10.1021/acsbiomaterials.2c00509
ACS Biomater. Sci. Eng. XXXX, XXX, XXX−XXX

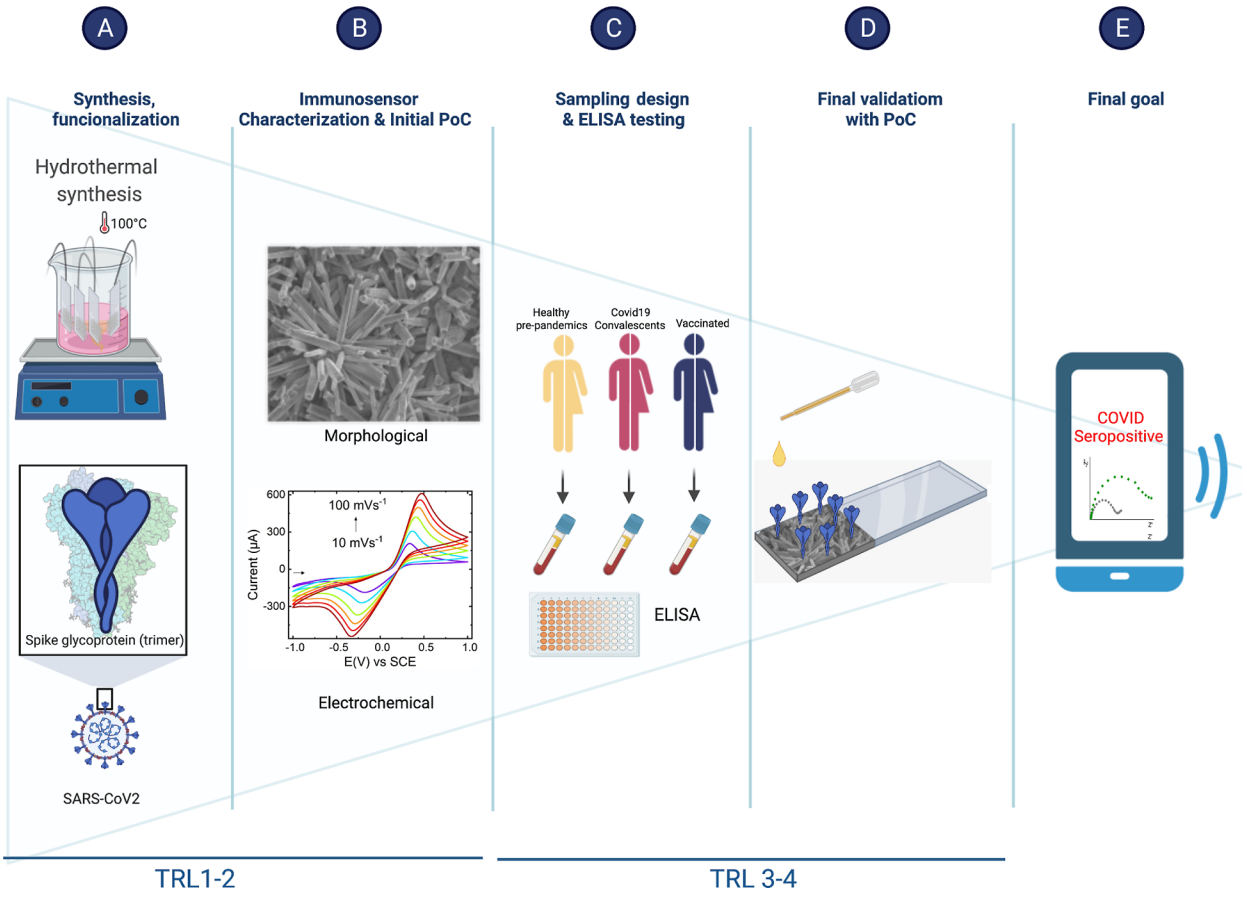

Figure 6. Development and validation of the electrochemical ZnONR immunosensors for anti-SARS-CoV-2 antibody detection. (A) Basic science research. Hydrothermal synthesis of ZnONRs, FTO (tluorine tin oxide) functionalization with viral spike protein, and optimization of sensor architecture and (B) prototype characterization. Morphological, spectroscopic, and electrochemical characterization was performed before and after the biological modification of ZnONR-modified FTO electrodes and (C) concept validation. Sampling design, collection, and confirmation of the clinical status by anti-S IgG ELISA serological analysis. (D) Final validation with the proof of concept. Clinical serum samples from healthy pre-COVID19 individuals, convalescents, and vaccinated patients were applied on the ZnO electrode surface for anti-COVID19 antibody detection and (E) final project goal.

cutoff, suggesting that the antibody titers present in the analyzed samples are relatively low and consistent with a negative ELISA result. Previous studies reported deficient production of vaccine-induced antibody titers after CoronaVac application, especially among elderly and immunocompromised individuals.[12−15] Our results demonstrate that the ZnONRs/spike immunosensor can detect the anti-SARS-CoV-2 spike protein antibody in individuals vaccinated with CoronaVac. This point-of-care technology can specifically aid public health actions in assessing humoral immune response post-COVID-19 vaccination in the countries where this vaccine is applied.

ZnONRs/Spike Immunosensor Detection Performance Analysis. To further explore the potential of our detection system, we use the ROC curve analysis to graphically evaluate the ZnONRs/spike immunosensor detection test (Figure 5B). ROC analysis is a valuable tool for assessing the performance of diagnostic tests and, more generally, for evaluating the accuracy of a statistical model that classifies subjects into one of the two categories, diseased or non-diseased. The area under the ROC curve (AUC) is an overall summary of diagnostic accuracy. The AUC equals 0.5 when the ROC curve corresponds to random chance and 1.0 for perfect accuracy.[119,120]

The ZnONRs/spike immunosensor detection test presented an AUC of 0.9081, evidencing the high accuracy of this assay. Therefore, the developed ZnO detection system offers a viable alternative method for detecting anti-SARS-CoV-2 antibodies in human serum and has a potential application in estimating the prevalence of the SARS-CoV-2 antibodies in a given population. Data acquired from conventional ELISA anti-spike and ZnONRs/spike immunosensor were compared and correlated using Spearman rank correlation (Figure 5C). This correlation coefficient represents the power of the putative linear association among such variables.[121] The spearman coefficient ranged from −1 to 1. Values close to 1 indicate a strong and positive correlation, values relative to −1 indicate a strong, negative correlation, and values close to zero indicate no linear correlation.[122] In our analysis, a correlation coefficient of 0.507 was obtained, showing a positive and moderate correlation between the data obtained using conventional ELISA test and our novel ZnONRs/spike immunosensor. Considering the differences in the biological samples and readout approaches, a result of a moderate correlation with a relevant *P*-value is encouraging. Since different ELISA tests detect anti-S IgG, the ZnONRs/spike immunosensor is a direct assay designed to detect total specific antibodies against COVID-19 without needing a secondary

https://doi.org/10.1021/acsbiomaterials.2c00509
ACS Biomater. Sci. Eng. XXXX, XXX, XXX−XXX

antibody that specifically binds the species and class (isotype) of the primary antibody. This feature might be an added advantage for the other immunological detection of COVID19 in different animal species.

Evaluation of S Protein Concentration, Reproducibility, and Stability. Studying the impact of S protein concentration as the receptor molecule is critical for better biosensor design and performance. Different concentrations of S protein were immobilized in the range of 1 to 7 μg mL^{-1}. The EIS response was measured to monitor each electrode signal in triple experiments, using a $[Fe(CN)_6]^{4-/3-}$ solution as the redox probe. Response signal growing was explicitly stopped when the concentration of spike protein was over 4 μg mL^{-1} (Figure S7A), after which device response was linear, indicating the maximum amount of protein that could be absorbed on the electrode surface. Based on this performance, 4 μg mL^{-1} was selected as the ideal concentration in subsequent experiments.

Independent data from five modified electrodes were acquired using a pool of serum samples of COVID-19 convalescent and pre-pandemic individuals, respectively, to determine the immunosensor's reproducibility (Figure S7B). The relative standard deviation (RSD) measurements were 3.11% for pre-pandemic samples and 2.14% (for convalescent individuals), demonstrating outstanding reproducibility of the biodevice. Moreover, the response of the electrode FTO-ZnO/spike/Gly was measured for 10 different electrodes (Figure S7C), obtaining an RSD of 3.20%, validating that the proposed immunosensor has good reproducibility. For this purpose, the EIS response was measured using a $[Fe(CN)_6]^{4-/3-}$ solution as the redox probe.

The modified electrode was incubated with a serum sample of convalescent individuals (1:500 v/v) and stored at 4 °C to estimate the long-term stability of the device. The sensor showed around an 8.4% change in the impedance response after 15 days (Figure S7D).

In brief, all accomplished developmental phases of the ZnO immunosensor are represented in the schematic diagram (Figure 6). Each column corresponds to a step forward along with the product development and represents an increasing score along with the technology readiness level scale (TRL). The lower line indicates the work already performed and relates to the technology maturity level (TRL) already achieved in the project. The work described here moves the project from the beginning of TRL1 (basic science research) to TRL4 (final validation completion with the proof of concept). Our prospects are to adapt the current technology to be portable for on-site use, allowing the connection of mobile devices to facilitate the detection of COVID-19 antibodies since the future of public health is likely to become increasingly digital.

CONCLUSIONS

In this work, we have successfully developed a ZnONRs/spike immunosensor to detect anti-SARS-CoV-2 antibodies quickly. The fabricated electrode detected antibodies against SARS-CoV-2 spike protein in serum samples in about 5 min and showed a sensitivity of 88.7% and a specificity of 100%. No cross-reactivity with other common coronaviruses was found. The ZnONRs/spike immunosensor is easy to produce and employ, even though the bioreceptor component of the electrode, SARS-CoV-2 recombinant trimeric spike protein, has a high production cost as it requires expensive mammalian cell expression systems. The electrode's manufacturing cost is relatively cheap, making it a great alternative. The biosensor results revealed a strong concordance with the conventional ELISA test results or even more sensitivity since some of the tested serum samples were considered negative using ELISA and positively detected in our sensor. The novel ZnO-based biosensing platform has shown the potential to evaluate the humoral immune response in COVID-19 convalescent individuals or post-COVID-19 vaccination, supporting efforts for immunosurveillance, aiding the control of future global waves of regional outbreaks of SARS-CoV-2 across the world. The immunosensor presented an AUC of 0.9081, indicating the high accuracy of the assay. The biosensing system is highly reproducible and stable for a practical application (around 15 days). Furthermore, this nanostructured electrode architecture is flexible. It shows great potential for other diagnostic and biomedical applications since the sensor technology can be easily customized using different biomolecules on the ZnONRs or other target analytes.

ASSOCIATED CONTENT

Supporting Information

The Supporting Information is available free of charge at https://pubs.acs.org/doi/10.1021/acsbiomaterials.2c00509.

Electrochemical behavior of FTO electrodes; FTIR spectra at each fabrication stage of the electrodes; XPS spectra; quantification detection of mAb anti-SARS-CoV spike protein; ELISA assay for pre-pandemic, convalescents, and vaccinated individuals; ELISA assay HCoVs; optimization, reproducibility, and stability of the immunosensor; fitted parameters of the Nyquist impedance plot at each assembly stage of the ZnONRs immunosensor; and performance comparison of the Covid-19 serological tests (PDF)

AUTHOR INFORMATION

Corresponding Author

Wendel A. Alves − *Centro de Ciências Naturais e Humanas, Universidade Federal do ABC, Santo André, São Paulo 09210-580, Brazil;* orcid.org/0000-0002-8394-2751; Email: wendel.alves@ufabc.edu.br

Authors

Freddy A. Nunez − *Centro de Ciências Naturais e Humanas, Universidade Federal do ABC, Santo André, São Paulo 09210-580, Brazil*

Ana C. H. Castro − *Centro de Ciências Naturais e Humanas, Universidade Federal do ABC, Santo André, São Paulo 09210-580, Brazil*

Vivian L. de Oliveira − *Centro de Ciências Naturais e Humanas, Universidade Federal do ABC, Santo André, São Paulo 09210-580, Brazil; Laboratório de Imunologia, LIM19, Instituto do Coração (InCor), Hospital das Clínicas da Faculdade de Medicina da Universidade de São Paulo (HCFMUSP), São Paulo, São Paulo 05403-900, Brazil;* orcid.org/0000-0003-2523-0374

Ariane C. Lima − *Departamento de Clínica Médica, Disciplina de Alergia e Imunologia Clínica, Faculdade de Medicina da Universidade de São Paulo, São Paulo, São Paulo 01246-903, Brazil*

Jamille R. Oliveira − *Departamento de Clínica Médica, Disciplina de Alergia e Imunologia Clínica, Faculdade de*

https://doi.org/10.1021/acsbiomaterials.2c00509
ACS Biomater. Sci. Eng. XXXX, XXX, XXX−XXX

Medicina da Universidade de São Paulo, São Paulo, São Paulo 01246-903, Brazil; orcid.org/0000-0002-4993-5494

Giuliana X. de Medeiros − *Departamento de Clínica Médica, Disciplina de Alergia e Imunologia Clínica, Faculdade de Medicina da Universidade de São Paulo, São Paulo, São Paulo 01246-903, Brazil*

Greyce L. Sasahara − *Laboratório de Imunologia, LIM19, Instituto do Coração (InCor), Hospital das Clínicas da Faculdade de Medicina da Universidade de São Paulo (HCFMUSP), São Paulo, São Paulo 05403-900, Brazil*

Keity S. Santos − *Laboratório de Imunologia, LIM19, Instituto do Coração (InCor), Hospital das Clínicas da Faculdade de Medicina da Universidade de São Paulo (HCFMUSP), São Paulo, São Paulo 05403-900, Brazil; Departamento de Clínica Médica, Disciplina de Alergia e Imunologia Clínica, Faculdade de Medicina da Universidade de São Paulo, São Paulo, São Paulo 01246-903, Brazil;* orcid.org/0000-0001-5271-4011

Alexandre J. C. Lanfredi − *Centro de Engenharia, Modelagem e Ciências Sociais Aplicadas, Universidade Federal do ABC, Santo André, São Paulo 09210-580, Brazil;* orcid.org/0000-0002-8530-8826

Complete contact information is available at: https://pubs.acs.org/10.1021/acsbiomaterials.2c00509

Author Contributions

F.A.N: methodology, validation, investigation, and writing—original draft. W.A.A., V.L.d.O., and A.C.H.C: conceived the sensing strategy, designed the study, conducted data curation, writing—review and editing, and visualization. A.J.C.L. and F.A.N: conducted SEM and XPS acquirement and analysis. F.A.N and W.A.A: conducted FTIR acquirement and analysis. J.R.O. and A.C.L.: performed ELISA Tests. G.X.d.M and G.L.S: processed laboratory human samples. K.S.S.: immunological resources. W.A.A.: supervising and funding acquisition.

Notes

The authors declare no competing financial interest.

■ ACKNOWLEDGMENTS

This work was supported by FAPESP (#2017/02317-2), CNPq (#304389/2019-6 and #407951/2021-0), CAPES (#88881.504639/2020-01), and the National Institute of Science and Technology in Bioanalytics (FAPESP #2014/50867-3 and CNPq #465389/2014-7) grants. The authors are grateful to the Multiuser Central Facilities at UFABC. We thank the Cell Culture Engineering Laboratory at COPPE/UFRJ for the recombinant protein S of SARS-CoV-2. Figures were created with BioRender.com.

■ ABBREVIATIONS

S Protein, recombinant trimeric spike protein; ELISA, enzyme-linked immunosorbent assay; PCR, polymerase chain reaction; ZnONRs, zinc oxide nanorods; LFA, immunochromatographic lateral flow assay; HMTA, hexamethylenetetramine; FTO, fluorine-doped tin oxide; EIS, electrochemical impedance spectroscopy; CV, cyclic voltammetry; SWV, square-wave voltammetry; ROC, received-operating characteristic curve; AUC, area under the ROC curve

■ REFERENCES

(1) WHO. WHO Coronavirus (COVID-19) Dashboard. https://covid19.who.int/(accessed 13 04, 2022).

(2) Basto-Abreu, A.; Carnalla, M.; Torres-Ibarra, L.; Romero-Martínez, M.; Martínez-Barnetche, J.; López-Martínez, I.; Aparicio-Antonio, R.; Shamah-Levy, T.; Alpuche-Aranda, C.; Rivera, J. A.; Barrientos-Gutierrez, T.; Cuevas-Nasu, L.; Gaona-Pineda, E. B.; Ávila-Arcos, M. A.; Reyes-Sánchez, F.; Torres-Álvarez, R.; López-Olmedo, N.; Vidaña-Perez, D.; González-Morales, R.; Barrera-Nuñez, D.; Perez-Ferrer, C.; Gaspar-Castillo, C.; Stern, D.; Canto-Osorio, F.; Sanchez-Pájaro, A. Nationally Representative SARS-CoV-2 Antibody Prevalence Estimates after the First Epidemic Wave in Mexico. *Nat. Commun.* **2022**, *13*, 589.

(3) Lalwani, P.; Salgado, B. B.; Filho, I. V. P.; da Silva, D. S. S.; de Morais, T. B. do N.; Jordão, M. F.; Barbosa, A. R. C.; Cordeiro, I. B.; Neto, J. N. de S.; de Assunção, E. N.; dos Santos, R. O.; Carvalho, N. O.; Sobrinho, W. B. S.; da Costa, C. F.; de Souza, P. E.; de Albuquerque, B. C.; Ganoza, C. A.; Araujo-Castillo, R. v.; Filho, S. A.; Lalwani, J. D. B. SARS-CoV-2 Seroprevalence and Associated Factors in Manaus, Brazil: Baseline Results from the DETECTCoV-19 Cohort Study. *Int. J. Infect. Dis.* **2021**, *110*, 141−150.

(4) Rostami, A.; Sepidarkish, M.; Leeflang, M. M.; Riahi, S.; Nourollahpour Shiadeh, M.; Esfandyari, S.; Mokdad, A. H.; Hotez, P. J.; Gasser, R. B.; author Robin Gasser, C. B. SARS-CoV-2 seroprevalence worldwide: a systematic review and meta-analysis. *Clin. Microbiol. Infect.* **2021**, *27*, 331−340.

(5) Wu, M.; Wall, E. C.; Carr, E. J.; Harvey, R.; Townsley, H.; Mears, H. v.; Adams, L.; Kjaer, S.; Kelly, G.; Warchal, S.; Sawyer, C.; Kavanagh, C.; Queval, C. J.; Ngai, Y.; Hatipoglu, E.; Ambrose, K.; Hindmarsh, S.; Beale, R.; Gamblin, S.; Howell, M.; Kassiotis, G.; Libri, V.; Williams, B.; Gandhi, S.; Swanton, C.; Bauer, D. L. Three-Dose Vaccination Elicits Neutralising Antibodies against Omicron. *Lancet* **2022**, *399*, 715−717.

(6) Collie, S.; Champion, J.; Moultrie, H.; Bekker, L.-G.; Gray, G. Effectiveness of BNT162b2 Vaccine against Omicron Variant in South Africa. *N. Engl. J. Med.* **2022**, *386*, 494−496.

(7) Vanaparthy, R.; Mohan, G.; Vasireddy, D.; Atluri, P. Review of Covid-19 Viral Vector-Based Vaccines and Covid-19 Variants. *Infez. Med.* **2021**, *29*, 328−338.

(8) Stamatatos, L.; Czartoski, J.; Wan, Y. H.; Homad, L. J.; Rubin, V.; Glantz, H.; Neradilek, M.; Seydoux, E.; Jennewein, M. F.; MacCamy, A. J.; Feng, J.; Mize, G.; de Rosa, S. C.; Lemos, A.; Cohen, M. P.; Moodie, K. W.; McElrath, Z.; McGuire, M. J.; McGuire, A. T. MRNA Vaccination Boosts Cross-Variant Neutralizing Antibodies Elicited by SARS-CoV-2 Infection. *Science* **2021**, *372*, 1413−1418.

(9) Hitchings, M. D. T.; Ranzani, O. T.; Torres, M. S. S.; de Oliveira, S. B.; Almiron, M.; Said, R.; Borg, R.; Schulz, W. L.; de Oliveira, R. D.; da Silva, P. V.; de Castro, D. B.; Sampaio, V. de S.; de Albuquerque, B. C.; Ramos, T. C. A.; Fraxe, S. H. H.; da Costa, C. F.; Naveca, F. G.; Siqueira, A. M.; de Araújo, W. N.; Andrews, J. R.; Cummings, D. A. T.; Ko, A. I.; Croda, J. Effectiveness of CoronaVac among Healthcare Workers in the Setting of High SARS-CoV-2 Gamma Variant Transmission in Manaus, Brazil: A Test-Negative Case-Control Study. *Lancet Reg. Health. Am.* **2021**, *1*, 100025.

(10) Li, J.; Hou, L.; Guo, X.; Jin, P.; Wu, S.; Zhu, J.; Pan, H.; Wang, X.; Song, Z.; Wan, J.; Cui, L.; Li, J.; Chen, Y.; Wang, X.; Jin, L.; Liu, J.; Shi, F.; Xu, X.; Zhu, T.; Chen, W.; Zhu, F. Heterologous AD5-NCOV plus CoronaVac versus Homologous CoronaVac Vaccination: A Randomized Phase 4 Trial. *Nat. Med.* **2022**, *28*, 401−409.

(11) Jara, A.; Undurraga, E. A.; González, C.; Paredes, F.; Fontecilla, T.; Jara, G.; Pizarro, A.; Acevedo, J.; Leo, K.; Leon, F.; Sans, C.; Leighton, P.; Suárez, P.; García-Escorza, H.; Araos, R. Effectiveness of an Inactivated SARS-CoV-2 Vaccine in Chile. *N. Engl. J. Med.* **2021**, *385*, 875−884.

(12) Medeiros, G. X.; Sasahara, G. L.; Magawa, J. Y.; Nunes, J. P. S.; Bruno, F. R.; Kuramoto, A. C.; Almeida, R. R.; Ferreira, M. A.; Scagion, G. P.; Candido, E. D.; Leal, F. B.; Oliveira, D. B. L.; Durigon, E. L.; Silva, R. C. v.; Rosa, D. S.; Boscardin, S. B.; Coelho, V.; Kalil, J.; Santos, K. S.; Cunha-Neto, E. Reduced T Cell and Antibody

Responses to Inactivated Coronavirus Vaccine Among Individuals Above 55 Years Old. *Front. Immunol.* **2022**, *13*, 812126.
(13) Karamese, M.; Tutuncu, E. E. The Effectiveness of Inactivated SARS-CoV-2 Vaccine (CoronaVac) on Antibody Response in Participants Aged 65 Years and Older. *J. Med. Virol.* **2022**, *94*, 173−177.
(14) Seyahi, E.; Bakhdiyarli, G.; Oztas, M.; Kuskucu, M. A.; Tok, Y.; Sut, N.; Ozcifci, G.; Ozcaglayan, A.; Balkan, I. I.; Saltoglu, N.; Tabak, F.; Hamuryudan, V. Antibody Response to Inactivated COVID-19 Vaccine (CoronaVac) in Immune-Mediated Diseases: A Controlled Study among Hospital Workers and Elderly. *Rheumatol. Int.* **2021**, *41*, 1429−1440.
(15) Vacharathit, V.; Aiewsakun, P.; Manopwisedjaroen, S.; Srisaowakarn, C.; Laopanupong, T.; Ludowyke, N.; Phuphuakrat, A.; Setthaudom, C.; Ekronarongchai, S.; Srichatrapimuk, S.; Wongsirisin, P.; Sangrajrang, S.; Imsuwansri, T.; Kirdlarp, S.; Nualkaew, S.; Sensorn, I.; Sawaengdee, W.; Wichukchinda, N.; Sungkanuparph, S.; Chantratita, W.; Kunakorn, M.; Rojanamatin, J.; Hongeng, S.; Thitithanyanont, A. CoronaVac Induces Lower Neutralising Activity against Variants of Concern than Natural Infection. *Lancet Infect. Dis.* **2021**, *21*, 1352−1354.
(16) Sethuraman, N.; Jeremiah, S. S.; Ryo, A. Interpreting Diagnostic Tests for SARS-CoV-2. *JAMA* **2020**, *323*, 2249−2251.
(17) Liu, P. P.; Zong, Y.; Jiang, S. P.; Jiao, Y. J.; Yu, X. J. Development of a Nucleocapsid Protein-Based ELISA for Detection of Human IgM and IgG Antibodies to SARS-CoV-2. *ACS Omega* **2021**, *6*, 9667−9671.
(18) Yadav, S.; Sadique, M. A.; Ranjan, P.; Kumar, N.; Singhal, A.; Srivastava, A. K.; Khan, R. SERS Based Lateral Flow Immunoassay for Point-of-Care Detection of SARS-CoV-2 in Clinical Samples. *ACS Appl. Bio Mater.* **2021**, *4*, 2974−2995.
(19) Ditte, K.; Nguyen Le, T. A.; Ditzer, O.; Sandoval Bojorquez, D. I.; Chae, S.; Bachmann, M.; Baraban, L.; Lissel, F. Rapid Detection of SARS-CoV-2 Antigens and Antibodies Using OFET Biosensors Based on a Soft and Stretchable Semiconducting Polymer. *ACS Biomater. Sci. Eng.* **2021**, DOI: 10.1021/acsbiomaterials.1c00727.
(20) Funari, R.; Chu, K. Y.; Shen, A. Q. Detection of Antibodies against SARS-CoV-2 Spike Protein by Gold Nanospikes in an Opto-Microfluidic Chip. *Biosens. Bioelectron.* **2020**, *169*, 112578.
(21) Mahshid, S. S.; Flynn, S. E.; Mahshid, S. The Potential Application of Electrochemical Biosensors in the COVID-19 Pandemic: A Perspective on the Rapid Diagnostics of SARS-CoV-2. *Biosens. Bioelectron.* **2021**, *176*, 112905.
(22) da Silva, S. J. R.; da Silva, C. T. A.; Guarines, K. M.; Mendes, R. P. G.; Pardee, K.; Kohl, A.; Pena, L. Clinical and Laboratory Diagnosis of SARS-CoV-2, the Virus Causing COVID-19. *ACS Infect. Dis.* **2020**, *6*, 2319−2336.
(23) Parihar, A.; Ranjan, P.; Sanghi, S. K.; Srivastava, A. K.; Khan, R. Point-of-Care Biosensor-Based Diagnosis of COVID-19 Holds Promise to Combat Current and Future Pandemics. *ACS Appl. Bio Mater.* **2020**, *3*, 7326−7343.
(24) Zhu, X.; Yuri, I.; Gan, X.; Suzuki, I.; Li, G. Electrochemical Study of the Effect of Nano-Zinc Oxide on Microperoxidase and Its Application to More Sensitive Hydrogen Peroxide Biosensor Preparation. *Biosens. Bioelectron.* **2007**, *22*, 1600−1604.
(25) Barbosa, H. P.; Araújo, D. A. G.; Pradela-Filho, L. A.; Takeuchi, R. M.; de Lima, R. G.; Ferrari, J. L.; Sousa Góes, M.; dos Santos, A. L. . *Zinc Oxide as a Multifunctional Material: From Biomedical Applications to Energy Conversion and Electrochemical Sensing*; Springer, 2021; Vol. *55*, pp 251−305.
(26) Fortunato, E.; Gonçalves, A.; Pimentel, A.; Barquinha, P.; Gonçalves, G.; Pereira, L.; Ferreira, I.; Martins, R. Zinc Oxide, a Multifunctional Material: From Material to Device Applications. *Appl. Phys. A* **2009**, *96*, 197−205.
(27) Shetti, N. P.; Bukkitgar, S. D.; Reddy, K. R.; Reddy, C. V.; Aminabhavi, T. M. ZnO-Based Nanostructured Electrodes for Electrochemical Sensors and Biosensors in Biomedical Applications. *Biosens. Bioelectron.* **2019**, *141*, 111417.
(28) Dien, N. D. Preparation of Various Morphologies of ZnO Nanostructure through Wet Chemical Methods. *Adv. Mater. Sci.* **2019**, *4*, 1−5.
(29) Wojnarowicz, J.; Chudoba, T.; Lojkowski, W. A Review of Microwave Synthesis of Zinc Oxide Nanomaterials: Reactants, Process Parameters and Morphologies. *Nanomaterials* **2020**, *10*, 1086.
(30) Ellmer, K. Magnetron Sputtering of Transparent Conductive Zinc Oxide: Relation between the Sputtering Parameters and the Electronic Properties. *J. Phys. D: Appl. Phys.* **2000**, *33*, R17.
(31) Maruyama, T.; Shionoya, J. Zinc Oxide Thin Films Prepared by Chemical Vapour Deposition from Zinc Acetate. *J. Mater. Sci. Lett.* **1992**, *11*, 170−172.
(32) Sbrockey, N. M.; Ganesan, S. ZnO thin films by MOCVD. *III-Vs Rev.* **2004**, *17*, 23−25.
(33) Black, K.; Chalker, P. R.; Jones, A. C.; King, P. J.; Roberts, J. L.; Heys, P. N. A New Method for the Growth of Zinc Oxide Nanowires by MOCVD Using Oxygen-Donor Adducts of Dimethylzinc. *Chem. Vap. Deposition* **2010**, *16*, 106−111.
(34) Wang, X.; Li, X.; Zhang, Q.; Lu, Z.; Song, H.; Wang, Y. Electrodeposition of ZnO Nanorods with Synergistic Photocatalytic and Self-Cleaning Effects. *J. Electron. Mater.* **2021**, *50*, 4954−4961.
(35) Kumar, M.; Sasikumar, C. Electrodeposition of Nanostructured ZnO Thin Film: A Review. *Am. J. Mater. Sci.* **2014**, *2*, 18−23.
(36) Inguanta, R.; Garlisi, C.; Spanò, T.; Piazza, S.; Sunseri, C. Growth and Photoelectrochemical Behaviour of Electrodeposited ZnO Thin Films for Solar Cells. *J. Appl. Electrochem.* **2013**, *43*, 199−208.
(37) Ridhuan, N. S.; Abdul Razak, K.; Lockman, Z. Fabrication and Characterization of Glucose Biosensors by Using Hydrothermally Grown ZnO Nanorods. *Sci. Rep.* **2018**, *8*, 13722.
(38) Dai, Z.; Shao, G.; Hong, J.; Bao, J.; Shen, J. Immobilization and Direct Electrochemistry of Glucose Oxidase on a Tetragonal Pyramid-Shaped Porous ZnO Nanostructure for a Glucose Biosensor. *Biosens. Bioelectron.* **2009**, *24*, 1286−1291.
(39) Palomera, N.; Balaguera, M.; Arya, S. K.; Hernández, S.; Tomar, M. S.; Ramírez-Vick, J. E.; Singh, S. P. Zinc Oxide Nanorods Modified Indium Tin Oxide Surface for Amperometric Urea Biosensor. *J. Nanosci. Nanotechnol.* **2011**, *11*, 6683−6689.
(40) Tak, M.; Gupta, V.; Tomar, M. Flower-like ZnO Nanostructure Based Electrochemical DNA Biosensor for Bacterial Meningitis Detection. *Biosens. Bioelectron.* **2014**, *59*, 200−207.
(41) Israr, M. Q.; Sadaf, J. R.; Asif, M. H.; Nur, O.; Willander, M.; Danielsson, B. Potentiometric Cholesterol Biosensor Based on ZnO Nanorods Chemically Grown on Ag Wire. *Thin Solid Films* **2010**, *519*, 1106−1109.
(42) Jang, Y.; Park, J.; Pak, Y. K.; Pak, J. J. Immunosensor Based on the ZnO Nanorod Networks for the Detection of H1N1 Swine Influenza Virus. *J. Nanosci. Nanotechnol.* **2012**, *12*, 5173−5177.
(43) Park, J.; You, X.; Jang, Y.; Nam, Y.; Kim, M. J.; Min, N. K.; Pak, J. J. ZnO Nanorod Matrix Based Electrochemical Immunosensors for Sensitivity Enhanced Detection of Legionella Pneumophila. *Sens. Actuators, B* **2014**, *200*, 173−180.
(44) Tereshchenko, A.; Fedorenko, V.; Smyntyna, V.; Konup, I.; Konup, A.; Eriksson, M.; Yakimova, R.; Ramanavicius, A.; Balme, S.; Bechelany, M. ZnO Films Formed by Atomic Layer Deposition as an Optical Biosensor Platform for the Detection of Grapevine Virus A-Type Proteins. *Biosens. Bioelectron.* **2017**, *92*, 763−769.
(45) Gasparotto, G.; Costa, J. P. C.; Costa, P. I.; Zaghete, M. A.; Mazon, T. Electrochemical Immunosensor Based on ZnO Nanorods-Au Nanoparticles Nanohybrids for Ovarian Cancer Antigen CA-125 Detection. *Mater. Sci. Eng., C* **2017**, *76*, 1240−1247.
(46) Liu, A.; Yin, K.; Mi, L.; Ma, M.; Liu, Y.; Li, Y.; Wei, W.; Zhang, Y.; Liu, S. A Novel Photoelectrochemical Immunosensor by Integration of Nanobody and ZnO Nanorods for Sensitive Detection of Nucleoside Diphosphatase Kinase-A. *Anal. Chim. Acta* **2017**, *973*, 82−90.
(47) Martins, B. R.; Sampaio, T. M.; de Farias, A. K. S. R.; de Paula Martins, R. de P.; Teixeira, R. R.; Oliveira, R. T. S.; Oliveira, C. J. F.; da Silva, M. V.; Rodrigues, V.; Dantas, N. O.; Espindola, F. S.; Silva,

https://doi.org/10.1021/acsbiomaterials.2c00509
ACS Biomater. Sci. Eng. XXXX, XXX, XXX−XXX

A. C. A.; Alves-Balvedi, R. P. Immunosensor Based on Zinc Oxide Nanocrystals Decorated with Copper for the Electrochemical Detection of Human Salivary Alpha-Amylase. *Micromachines* **2021**, *12*, 657.
(48) Vabbina, P. K.; Kaushik, A.; Pokhrel, N.; Bhansali, S.; Pala, N. Electrochemical Cortisol Immunosensors Based on Sonochemically Synthesized Zinc Oxide 1D Nanorods and 2D Nanoflakes. *Biosens. Bioelectron.* **2015**, *63*, 124−130.
(49) Tabatabaei, M. K.; Fard, H. G.; Koohsorkhi, J.; Mohammadnejad Arough, J. High-performance Immunosensor for Urine Albumin Using Hybrid Architectures of ZnO Nanowire/Carbon Nanotube. *IET Nanobiotechnol.* **2020**, *14*, 126−132.
(50) Koike, K.; Mukai, K.; Onaka, T.; Maemoto, T.; Sasa, S.; Yano, M. A Potentiometric Immunosensor Based on a ZnO Field-Effect Transistor. *Jpn. J. Appl. Phys.* **2014**, *53*, 05FF04.
(51) Dong, S.; Tong, M.; Zhang, D.; Huang, T. The strategy of nitrite and immunoassay human IgG biosensors based on ZnO@ZIF-8 and ionic liquid composite film. *Mater. Sci. Eng., C* **2017**, *251*, 650−657.
(52) Patella, B.; Moukri, N.; Regalbuto, G.; Cipollina, C.; Pace, E.; Di Vincenzo, S.; Aiello, G.; O'Riordan, A.; Inguanta, R. Electrochemical Synthesis of Zinc Oxide Nanostructures on Flexible Substrate and Application as an Electrochemical Immunoglobulin-G Immunosensor. *Materials* **2022**, *15*, 713.
(53) Yang, T.; Chen, M.; Kong, Q.; Luo, X.; Jiao, K. Toward DNA Electrochemical Sensing by Free-Standing ZnO Nanosheets Grown on 2D Thin-Layered MoS2. *Biosens. Bioelectron.* **2017**, *89*, 538−544.
(54) Wang, C.; Tan, X.; Chen, S.; Yuan, R.; Hu, F.; Yuan, D.; Xiang, Y. Highly-Sensitive Cholesterol Biosensor Based on Platinum-Gold Hybrid Functionalized ZnO Nanorods. *Talanta* **2012**, *94*, 263−270.
(55) Choi, M. S.; Na, H. G.; Shim, G. S.; Cho, J. H.; Kim, M. Y.; Kim, S. i.; Baek, S. H.; Jin, C.; Lee, K. H. Simple and Scalable Synthesis of Urchin-like ZnO Nanoparticles via a Microwave-Assisted Drying Process. *Ceram. Int.* **2021**, *47*, 14621−14629.
(56) Chang, T. H.; Lu, Y. C.; Yang, M. J.; Huang, J. W.; Linda Chang, P. F.; Hsueh, H. Y. Multibranched Flower-like ZnO Particles from Eco-Friendly Hydrothermal Synthesis as Green Antimicrobials in Agriculture. *J. Cleaner Prod.* **2020**, *262*, 121342.
(57) Phuruangrat, A.; Kuntalue, B.; Thongtem, S.; Thongtem, T. Hydrothermal Synthesis of Hexagonal ZnO Nanoplates Used for Photodegradation of Methylene Blue. *Optik* **2021**, *226*, 165949.
(58) Mwankemwa, B. S.; Malevu, T. D.; Sahini, M. G.; Vuai, S. A. Effects of Vertically Aligned ZnO Nanorods Surface Morphology on the Ambient-Atmosphere Fabricated Organic Solar Cells. *Results Mater.* **2022**, *14*, 100271.
(59) Chen, Y. X.; Zhao, X. Q.; Sha, B.; Chen, J. H. Stacking Fault Directed Growth of Thin ZnO Nanobelt. *Mater. Lett.* **2008**, *62*, 2369−2371.
(60) Kołodziejczak-Radzimska, A.; Jesionowski, T. Zinc Oxide-From Synthesis to Application: A Review. *Materials* **2014**, *7*, 2833−2881.
(61) Souza, J. S.; Carvalho, W. M.; Souza, F. L.; Ponce-de-Leon, C.; Bavykin, D. v.; Alves, W. A. Multihierarchical Electrodes Based on Titanate Nanotubes and Zinc Oxide Nanorods for Photoelectrochemical Water Splitting. *J. Mater. Chem. A* **2016**, *4*, 944−952.
(62) Elgrishi, N.; Rountree, K. J.; McCarthy, B. D.; Rountree, E. S.; Eisenhart, T. T.; Dempsey, J. L. A Practical Beginner's Guide to Cyclic Voltammetry. *J. Chem. Educ.* **2018**, *95*, 197−206.
(63) Huang, M. H.; Mao, S.; Feick, H.; Yan, H.; Wu, Y.; Kind, H.; Weber, E.; Russo, R.; Yang, P. Room-Temperature Ultraviolet Nanowire Nanolasers. *Science* **2001**, *292*, 1897−1899.
(64) Jindal, K.; Tomar, M.; Gupta, V. CuO Thin Film Based Uric Acid Biosensor with Enhanced Response Characteristics. *Biosens. Bioelectron.* **2012**, *38*, 11−18.
(65) Molaakbari, E.; Mostafavi, A.; Beitollahi, H.; Alizadeh, R. Synthesis of ZnO Nanorods and Their Application in the Construction of a Nanostructure-Based Electrochemical Sensor for Determination of Levodopa in the Presence of Carbidopa. *Analyst* **2014**, *139*, 4356−4364.
(66) Wang, J. *Analytical Electrochemistry*, 3rd ed.; Wiley, 2006.
(67) Al-Fandi, M. G.; Alshraiedeh, N. H.; Oweis, R. J.; Hayajneh, R. H.; Alhamdan, I. R.; Alabed, R. A.; Al-Rawi, O. F. Direct Electrochemical Bacterial Sensor Using ZnO Nanorods Disposable Electrode. *Sens. Rev.* **2018**, *38*, 326−334.
(68) Siddegowda, K. S.; Mahesh, B.; Chamaraja, N. A.; Roopashree, B.; Kumara Swamy, N.; Nanjundaswamy, G. S. Zinc Oxide Nanoparticles Supported on Multi-Walled Carbon Nanotube Modified Electrode for Electrochemical Sensing of a Fluoroquinolone Drug. *Electroanalysis* **2020**, *32*, 2183−2192.
(69) Batra, N.; Sharma, A.; Tomar, M.; Gupta, V. Efficient Detection of Total Cholesterol Using (ChEt-ChOx/ZnO/Pt/Si) Bioelectrode Based on ZnO Matrix. *Thin Solid Films* **2014**, *562*, 612−620.
(70) Hou, X.; Wang, L.; He, G.; Hao, J. Synthesis, Optical and Electrochemical Properties of ZnO Nanorod Hybrids Loaded with High-Density Gold Nanoparticles. *CrystEngComm* **2012**, *14*, 5158−5162.
(71) Zhan, F.; Yang, Y.; Liu, W.; Wang, K.; Li, W.; Li, J. Facile Synthesis of FeOOH Quantum Dots Modified ZnO Nanorods Films via a Metal-Solating Process. *ACS Sustainable Chem. Eng.* **2018**, *6*, 7789−7798.
(72) Ferrag, C.; Kerman, K. Grand Challenges in Nanomaterial-Based Electrochemical Sensors. *Front. Sens.* **2020**, *1*, 583822.
(73) Zucolotto, V. Specialty Grand Challenges in Biosensors. *Front. Sens.* **2020**, *1*, 3.
(74) Huang, Y.; Yang, C.; Xu, X.; Xu, W.; Liu, S. Structural and Functional Properties of SARS-CoV-2 Spike Protein: Potential Antivirus Drug Development for COVID-19. *Acta Pharmacol. Sin.* **2020**, *41*, 1141−1149.
(75) Viter, R.; Khranovskyy, V.; Starodub, N.; Ogorodniichuk, Y.; Gevelyuk, S.; Gertnere, Z.; Poletaev, N.; Yakimova, R.; Erts, D.; Smyntyna, V.; Ubelis, A. Application of Room Temperature Photoluminescence from ZnO Nanorods for Salmonella Detection. *IEEE Sens. J.* **2014**, *14*, 2028−2034.
(76) Rodrigues, J.; Pereira, S. O.; Santos, N. F.; Rodrigues, C.; Costa, F. M.; Monteiro, T. Insights on Luminescence Quenching of ZnO Tetrapods in the Detection of HCG. *Appl. Surf. Sci.* **2020**, *527*, 146813.
(77) Viter, R.; Savchuk, M.; Starodub, N.; Balevicius, Z.; Tumenas, S.; Ramanaviciene, A.; Jevdokimovs, D.; Erts, D.; Iatsunskyi, I.; Ramanavicius, A. Photoluminescence Immunosensor Based on Bovine Leukemia Virus Proteins Immobilized on the ZnO Nanorods. *Sens. Actuators, B* **2019**, *285*, 601−606.
(78) Zia, T. ul H.; Shah, A. ul H. A. Label-Free Photoelectrochemical Immunosensor Based on Sensitive Photocatalytic Surface of Sn Doped ZnO for Detection of Hepatitis C (HCV) Anticore MAbs 19D9D6. *Colloids Surf., A* **2021**, *630*, 127586.
(79) Almeida, R. M.; Ferrari, V. C.; Souza, J.; Souza, F. L.; Alves, W. A. Tailoring a Zinc Oxide Nanorod Surface by Adding an Earth-Abundant Cocatalyst for Induced Sunlight Water Oxidation. *ChemPhysChem* **2020**, *21*, 476−483.
(80) McPeak, K. M.; Le, T. P.; Britton, N. G.; Nickolov, Z. S.; Elabd, Y. A.; Baxter, J. B. Chemical Bath Deposition of ZnO Nanowires at Near-Neutral PH Conditions without Hexamethylenetetramine (HMTA): Understanding the Role of HMTA in ZnO Nanowire Growth. *Langmuir* **2011**, *27*, 3672−3677.
(81) Hsu, Y. F.; Xi, Y. Y.; Tam, K. H.; Djurišić, A. B.; Luo, J.; Ling, C. C.; Cheung, C. K.; Ng, A. M. C.; Chan, W. K.; Deng, X.; Beling, C. D.; Fung, S.; Cheah, K. W.; Fong, P. W. K.; Surya, C. C. Undoped P-Type ZnO Nanorods Synthesized by a Hydrothermal Method. *Adv. Funct. Mater.* **2008**, *18*, 1020−1030.
(82) Yan, X.; Li, Z.; Chen, R.; Gao, W. Template Growth of ZnO Nanorods and Microrods with Controllable Densities. *Cryst. Growth Des.* **2008**, *8*, 2406−2410.
(83) Mitra, S.; Patra, P.; Chandra, S.; Debnath, N.; Das, S.; Banerjee, R.; Kundu, S. C.; Pramanik, P.; Goswami, A. Porous ZnO Nanorod for Targeted Delivery of Doxorubicin: In Vitro and in Vivo Response for Therapeutic Applications. *J. Mater. Chem.* **2012**, *22*, 24145−24154.

https://doi.org/10.1021/acsbiomaterials.2c00509
ACS Biomater. Sci. Eng. XXXX, XXX, XXX−XXX

(84) Klochko, N.; Klepikova, K.; Kopach, V.; Tyukhov, I.; Starikov, V.; Sofronov, D.; Khrypunova, I.; Zhadan, D.; Petrushenko, S.; Dukarov, S.; Lyubov, V.; Kirichenko, M.; Khrypunova, A. Development of Semi-Transparent ZnO/FTO Solar Thermoelectric Nanogenerator for Energy Efficient Glazing. *Sol. Energy* **2019**, *184*, 230−239.
(85) Hernández-Paredes, J.; Glossman-Mitnik, D.; Esparza-Ponce, H. E.; Alvarez-Ramos, M. E.; Duarte-Moller, A. Band Structure, Optical Properties and Infrared Spectrum of Glycine−Sodium Nitrate Crystal. *J. Mol. Struct.* **2008**, *875*, 295−301.
(86) Aydın, E. B.; Aydln, M.; Sezginturk, M. K. New Impedimetric Sandwich Immunosensor for Ultrasensitive and Highly Specific Detection of Spike Receptor Binding Domain Protein of SARS-CoV-2. *ACS Biomater. Sci. Eng.* **2021**, *7*, 3874−3885.
(87) Martinez-Cuazitl, A.; Vazquez-Zapien, G. J.; Sanchez-Brito, M.; Limon-Pacheco, J. H.; Guerrero-Ruiz, M.; Garibay-Gonzalez, F.; Delgado-Macuil, R. J.; de Jesus, M. G. G.; Pereyra-Talamantes, M. A.; Mata-Miranda, A.; Mata-Miranda, M. M. ATR-FTIR Spectrum Analysis of Saliva Samples from COVID-19 Positive Patients. *Sci. Rep.* **2021**, *11*, 19980.
(88) Pramanik, A.; Gao, Y.; Patibandla, S.; Mitra, D.; McCandless, M. G.; Fassero, L. A.; Gates, K.; Tandon, R.; Chandra Ray, P. The Rapid Diagnosis and Effective Inhibition of Coronavirus Using Spike Antibody Attached Gold Nanoparticles. *Nanoscale Adv.* **2021**, *3*, 1588−1596.
(89) Zhao, S.; Qiao, X.; Chen, M.; Li, Y.; Wang, X.; Xu, Z.; Wu, Y.; Luo, X. D. Amino Acid-Based Antifouling Peptides for the Construction of Electrochemical Biosensors Capable of Assaying Proteins in Serum with Enhanced Stability. *ACS Sens.* **2022**, *7*, 1740−1746.
(90) Biswas, S.; Lan, Q.; Li, C.; Xia, X. H. Morphologically Flex Sm-MOF Based Electrochemical Immunosensor for Ultrasensitive Detection of a Colon Cancer Biomarker. *Anal. Chem.* **2022**, *94*, 3013−3019.
(91) Aerathupalathu Janardhanan, J.; Chen, Y. L.; Liu, C. T.; Tseng, H. S.; Wu, P. I.; She, J. W.; Hsiao, Y. S.; Yu, H. H. Sensitive Detection of Sweat Cortisol Using an Organic Electrochemical Transistor Featuring Nanostructured Poly(3,4-Ethylenedioxythiophene) Derivatives in the Channel Layer. *Anal. Chem.* **2022**, *94*, 7584−7593.
(92) Saáedi, A.; Yousefi, R.; Jamali-Sheini, F.; Zak, A. K.; Cheraghizade, M.; Mahmoudian, M. R.; Baghchesara, M. A.; Dezaki, A. S. XPS Studies and Photocurrent Applications of Alkali-Metals-Doped ZnO Nanoparticles under Visible Illumination Conditions. *Phys. E Low-dimens. Syst. Nanostruct.* **2016**, *79*, 113−118.
(93) Ahmad, R.; Tripathy, N.; Khan, M. Y.; Bhat, K. S.; Ahn, M. S.; Hahn, Y. B. Ammonium Ion Detection in Solution Using Vertically Grown ZnO Nanorod Based Field-Effect Transistor. *RSC Adv.* **2016**, *6*, 54836−54840.
(94) Al-Gaashani, R.; Radiman, S.; Daud, A. R.; Tabet, N.; Al-Douri, Y. XPS and Optical Studies of Different Morphologies of ZnO Nanostructures Prepared by Microwave Methods. *Ceram. Int.* **2013**, *39*, 2283−2292.
(95) Wu, Z. W.; Tyan, S. L.; Chen, H. H.; Huang, J. C. A.; Huang, Y. C.; Lee, C. R.; Mo, T. S. Temperature-Dependent Photoluminescence and XPS Study of ZnO Nanowires Grown on Flexible Zn Foil via Thermal Oxidation. *Superlattices Microstruct.* **2017**, *107*, 38−43.
(96) Das, J.; Pradhan, S. K.; Sahu, D. R.; Mishra, D. K.; Sarangi, S. N.; Nayak, B. B.; Verma, S.; Roul, B. K. Micro-Raman and XPS Studies of Pure ZnO Ceramics. *Physica B* **2010**, *405*, 2492−2497.
(97) Das, S. K.; Dickinson, C.; Lafir, F.; Brougham, D. F.; Marsili, E. Synthesis, Characterization and Catalytic Activity of Gold Nanoparticles Biosynthesized with Rhizopus Oryzae Protein Extract. *Green Chem.* **2012**, *14*, 1322−1334.
(98) Kehrer, M.; Duchoslav, J.; Hinterreiter, A.; Cobet, M.; Mehic, A.; Stehrer, T.; Stifter, D. XPS Investigation on the Reactivity of Surface Imine Groups with TFAA. *Plasma Processes Polym.* **2019**, *16*, 1800160.
(99) Rushworth, J. v.; Ahmed, A.; Griffiths, H. H.; Pollock, N. M.; Hooper, N. M.; Millner, P. A. A Label-Free Electrical Impedimetric Biosensor for the Specific Detection of Alzheimer's Amyloid-Beta Oligomers. *Biosens. Bioelectron.* **2014**, *56*, 83−90.
(100) Qi, P.; Wan, Y.; Zhang, D. Impedimetric Biosensor Based on Cell-Mediated Bioimprinted Films for Bacterial Detection. *Biosens. Bioelectron.* **2013**, *39*, 282−288.
(101) Layqah, L. A.; Eissa, S. An Electrochemical Immunosensor for the Corona Virus Associated with the Middle East Respiratory Syndrome Using an Array of Gold Nanoparticle-Modified Carbon Electrodes. *Mikrochim. Acta* **2019**, *186*, 224.
(102) Alafeef, M.; Dighe, K.; Moitra, P.; Pan, D. Rapid, Ultrasensitive, and Quantitative Detection of SARS-CoV-2 Using Antisense Oligonucleotides Directed Electrochemical Biosensor Chip. *ACS Nano* **2020**, *14*, 17028−17045.
(103) Lister, A. S. Validation of HPLC Methods in Pharmaceutical Analysis. *Sep. Sci. Technol.* **2005**, *6*, 191−217.
(104) Zhang, Z.; Wang, X.; Wei, X.; Zheng, S. W.; Lenhart, B. J.; Xu, P.; Li, J.; Pan, J.; Albrecht, H.; Liu, C. Multiplex Quantitative Detection of SARS-CoV-2 Specific IgG and IgM Antibodies Based on DNA-Assisted Nanopore Sensing. *Biosens. Bioelectron.* **2021**, *181*, 113134.
(105) Jiang, M.; Dong, T.; Han, C.; Liu, L.; Zhang, T.; Kang, Q.; Wang, P.; Zhou, F. Regenerable and High-Throughput Surface Plasmon Resonance Assay for Rapid Screening of Anti-SARS-CoV-2 Antibody in Serum Samples. *Anal. Chim. Acta* **2022**, *1208*, 339830.
(106) Yakoh, A.; Pimpitak, U.; Rengpipat, S.; Hirankarn, N.; Chailapakul, O.; Chaiyo, S. Paper-Based Electrochemical Biosensor for Diagnosing COVID-19: Detection of SARS-CoV-2 Antibodies and Antigen. *Biosens. Bioelectron.* **2021**, *176*, 112912.
(107) Qu, J.; Chenier, M.; Zhang, Y.; Xu, C. Q. A Microflow Cytometry-Based Agglutination Immunoassay for Point-of-Care Quantitative Detection of SARS-CoV-2 IgM and IgG. *Micromachines* **2021**, *12*, 433.
(108) Wright, P. F.; Nilsson, E.; Van Rooij, E. M.; Lelenta, M.; Jeggo, M. H. Standardisation and Validation of Enzyme-Linked Immunosorbent Assay Techniques for the Detection of Antibody in Infectious Disease Diagnosis. *Rev. Sci. Tech.* **1993**, *12*, 435−450.
(109) Frey, A.; Di Canzio, J.; Zurakowski, D. A Statistically Defined Endpoint Titer Determination Method for Immunoassays. *J. Immunol. Methods* **1998**, *221*, 35−41.
(110) Brodin, P. Immune Determinants of COVID-19 Disease Presentation and Severity. *Nat. Med.* **2021**, *27*, 28−33.
(111) Trevethan, R. Sensitivity, Specificity, and Predictive Values: Foundations, Pliabilities, and Pitfalls in Research and Practice. *Front. Public Health* **2017**, *5*, 307.
(112) Pewsner, D.; Battaglia, M.; Minder, C.; Marx, A.; Bucher, H. C.; Egger, M. Ruling a Diagnosis in or out with "SpPIn" and "SnNOut": A Note of Caution. *Br. Med. J.* **2004**, *329*, 209−213.
(113) Ravindran, R.; McReynolds, C.; Yang, J.; Hammock, B. D.; Ikram, A.; Ali, A.; Bashir, A.; Zohra, T.; Chang, W. L. W.; Hartigan-O'Connor, D. J.; Rashidi, H. H.; Khan, I. H. Immune Response Dynamics in COVID-19 Patients to SARS-CoV-2 and Other Human Coronaviruses. *PLoS One* **2021**, *16*, No. e0254367.
(114) Lombardi, A.; Bozzi, G.; Ungaro, R.; Villa, S.; Castelli, V.; Mangioni, D.; Muscatello, A.; Gori, A.; Bandera, A. Mini Review Immunological Consequences of Immunization With COVID-19 MRNA Vaccines: Preliminary Results. *Front. Immunol.* **2021**, *12*, 657711.
(115) Pollard, A. J.; Bijker, E. M. A Guide to Vaccinology: From Basic Principles to New Developments. *Nat. Rev. Immunol.* **2021**, *21*, 83−100.
(116) Cerqueira-Silva, T.; Andrews, J. R.; Boaventura, V. S.; Ranzani, O. T.; de Araújo Oliveira, V.; Paixão, E. S.; Júnior, J. B.; Machado, T. M.; Hitchings, M. D. T.; Dorion, M.; Lind, M. L.; Penna, G. O.; Cummings, D. A. T.; Dean, N. E.; Werneck, G. L.; Pearce, N.; Barreto, M. L.; Ko, A. I.; Croda, J.; Barral-Netto, M. Effectiveness of CoronaVac, ChAdOx1 NCoV-19, BNT162b2, and Ad26.COV2.S among Individuals with Previous SARS-CoV-2 Infection in Brazil: A Test-Negative, Case-Control Study. *Lancet Infect. Dis.* **2022**, *22*, 791.

https://doi.org/10.1021/acsbiomaterials.2c00509
ACS Biomater. Sci. Eng. XXXX, XXX, XXX−XXX

(117) Soysal, A.; Gönüllü, E.; Karabayir, N.; Alan, S.; Atici, S.; Yildiz, I.; Engin, H.; Çivilibal, M.; Karaböcüoğlu, M. Comparison of Immunogenicity and Reactogenicity of Inactivated SARS-CoV-2 Vaccine (CoronaVac) in Previously SARS-CoV-2 Infected and Uninfected Health Care Workers. *Hum. Vaccines Immunother.* **2021**, *17*, 1953344.
(118) Wang, Z.; Muecksch, F.; Schaefer-Babajew, D.; Finkin, S.; Viant, C.; Gaebler, C.; Hoffmann, H. H.; Barnes, C. O.; Cipolla, M.; Ramos, V.; Oliveira, T. Y.; Cho, A.; Schmidt, F.; Da Silva, J.; Bednarski, E.; Aguado, L.; Yee, J.; Daga, M.; Turroja, M.; Millard, K. G.; Jankovic, M.; Gazumyan, A.; Zhao, Z.; Rice, C. M.; Bieniasz, P. D.; Caskey, M.; Hatziioannou, T.; Nussenzweig, M. C. Naturally Enhanced Neutralizing Breadth against SARS-CoV-2 One Year after Infection. *Nature* **2021**, *595*, 426−431.
(119) Hajian-Tilaki, K. Receiver Operating Characteristic (ROC) Curve Analysis for Medical Diagnostic Test Evaluation. *Caspian J. Intern. Med.* **2013**, *4*, 627−635.
(120) Zou, K. H.; O'Malley, A. J.; Mauri, L. Receiver-Operating Characteristic Analysis for Evaluating Diagnostic Tests and Predictive Models. *Circulation* **2007**, *115*, 654−657.
(121) Mukaka, M. M. Statistics Corner: A Guide to Appropriate Use of Correlation Coefficient in Medical Research. *Malawi Med. J.* **2012**, *24*, 69−71.
(122) Schober, P.; Boer, C.; Schwarte, L. A. Correlation Coefficients: Appropriate Use and Interpretation. *Anesth. Analg.* **2018**, *126*, 1763−1768.

https://doi.org/10.1021/acsbiomaterials.2c00509
ACS Biomater. Sci. Eng. XXXX, XXX, XXX−XXX